Drag Coefficient and Its Sea State Dependence under Tropical Cyclones

XIAOHUI ZHOU,[a] TETSU HARA,[a] ISAAC GINIS,[a] ERIC D'ASARO,[b] JE-YUAN HSU,[c] AND BRANDON G. REICHL[d]

[a] *Graduate School of Oceanography, University of Rhode Island, Narragansett, Rhode Island*
[b] *Applied Physics Laboratory and School of Oceanography, University of Washington, Seattle, Washington*
[c] *Institute of Oceanography, National Taiwan University, Taipei, Taiwan*
[d] *NOAA/Geophysical Fluid Dynamics Laboratory, Princeton, New Jersey*

(Manuscript received 2 November 2021, in final form 14 March 2022)

ABSTRACT: The drag coefficient under tropical cyclones and its dependence on sea states are investigated by combining upper-ocean current observations [using electromagnetic autonomous profiling explorer (EM-APEX) floats deployed under five tropical cyclones] and a coupled ocean–wave (Modular Ocean Model 6–WAVEWATCH III) model. The estimated drag coefficient averaged over all storms is around 2–3 $\times 10^{-3}$ for wind speeds of 25–55 m s^{-1}. While the drag coefficient weakly depends on wind speed in this wind speed range, it shows stronger dependence on sea states. In particular, it is significantly reduced when the misalignment angle between the dominant wave direction and the wind direction exceeds about 45°, a feature that is underestimated by current models of sea state–dependent drag coefficient. Since the misaligned swell is more common in the far front and in the left-front quadrant of the storm (in the Northern Hemisphere), the drag coefficient also tends to be lower in these areas and shows a distinct spatial distribution. Our results therefore support ongoing efforts to develop and implement sea state–dependent parameterizations of the drag coefficient in tropical cyclone conditions.

KEYWORDS: Air-sea interaction; Wind stress; Tropical cyclones; Sea state; Momentum; Measurements; Numerical analysis/modeling

1. Introduction

The momentum transfer from the atmosphere to the ocean (or the wind stress) plays an important role in coupled atmosphere–ocean systems. The wind stress $\boldsymbol{\tau}_{\text{wind}}$ is normally parameterized by the neutral 10-m wind velocity $\mathbf{U}_{10N}$ (corrected for stability) and the drag coefficient (C_d) as $\boldsymbol{\tau}_{\text{wind}} = \rho_{\text{air}} C_d \mathbf{U}_{10N} U_{10N}$ in model simulations, where ρ_{air} is air density and $U_{10N} = |\mathbf{U}_{10N}|$. The drag coefficient C_d itself is often parameterized with U_{10N}, that is, the wind stress magnitude divided by air density, $|\boldsymbol{\tau}_{\text{wind}}|/\rho_{\text{air}} = u_*^2$, is assumed to be a function of U_{10N} only, where u_* is the friction velocity. Since the neutral wind speed profile is logarithmic inside the constant stress layer (but above the direct surface wave impacts), the drag coefficient can be expressed by the roughness length z_o as $C_d = \{\kappa/[\ln(z/z_0)]\}^2$, where $z = 10$ m and $\kappa = 0.4$ is the von Kármán constant, and the normalized roughness length (or the Charnock coefficient) is defined as $Z_{\text{ch}} = z_o g/u_*^2$ (Charnock 1955), where g is gravitational acceleration.

In low to medium wind speeds (approximately $U_{10N} <$ 20 m s^{-1}), previous studies show that C_d increases approximately linearly with wind (e.g., Large and Pond 1981; Donelan et al. 2004; Edson et al. 2013). In tropical cyclone (TC) conditions (approximately $U_{10N} >$ 25 m s^{-1}) C_d varies widely, roughly from 1.5 $\times 10^{-3}$ to 4.5 $\times 10^{-3}$ (e.g., Powell et al. 2003; Donelan et al. 2004; Sanford et al. 2011; Bryant and Akbar 2016; Hsu et al. 2019). Although some of this large variability of observed C_d is likely due to difficulties in measuring wind stress in extreme high-wind environments, it is also expected that the drag coefficient depends on factors other than U_{10N}, such as surface wave conditions (sea states).

Some previous studies suggest that the drag coefficient depends on sea states in addition to U_{10N} (e.g., Toba et al. 1990; Smith et al. 1992; Johnson et al. 1998; Taylor and Yelland 2001; Edson et al. 2013), including TC conditions (e.g., Holthuijsen et al. 2012; Chen et al. 2013; Reichl et al. 2014; Chen et al. 2020). Edson et al. (2013) (and studies cited in their study) suggest that the Charnock coefficient (Z_{ch}) decreases with the wave age (c_p/u_*, where c_p is the wave phase speed at the wave spectral peak) based on observations under low to medium wind conditions. Toba et al. (1990) show that Z_{ch} increases with the wave age if laboratory observations (with very small wave ages) are included. Some studies (Taylor and Yelland 2001; Edson et al. 2013) suggest that Z_{ch} increases with wave steepness (H_s/L_p, where H_s is the significant wave height and L_p is the wavelength at the wave spectral peak) in low to medium wind speeds.

Under TC conditions the sea state dependence of C_d has been addressed in very few observational studies. Holthuijsen et al. (2012) suggests that swells misaligned with wind impact the C_d estimation based on observations under Hurricane Bonnie. Several modeling studies have simulated the sea state–dependent C_d under TCs (Chen et al. 2013; Reichl et al. 2014; Chen et al. 2020). The model results typically show that C_d in the front-right quadrant of TCs is similar to or higher than that in the front-left quadrant (in the Northern

Denotes content that is immediately available upon publication as open access.

Supplemental information related to this paper is available at the Journals Online website: https://doi.org/10.1175/JPO-D-21-0246.s1.

Corresponding author: Xiaohui Zhou, xiaohui_zhou@uri.edu

DOI: 10.1175/JPO-D-21-0246.1

© 2022 American Meteorological Society. For information regarding reuse of this content and general copyright information, consult the AMS Copyright Policy (www.ametsoc.org/PUBSReuseLicenses).

Brought to you by NOAA Central Library | Unauthenticated | Downloaded 10/06/22 12:39 PM UTC

Hemisphere), which is very different from the spatial pattern observed by Holthuijsen et al. (2012). Swells misaligned with local wind may also cause the misalignment of the wind stress direction from the wind direction (Chen et al. 2013; Reichl et al. 2014; Hsu et al. 2019; Chen et al. 2020).

Although most studies estimate the drag coefficient in TC conditions using atmospheric measurements, some studies (Hsu et al. 2017, 2019; Sanford et al. 2011) estimate the wind stress using the upper-ocean current observations. Specifically, if the horizontal momentum equations for the ocean currents are integrated vertically from the surface down to a certain depth, where the turbulent stress is sufficiently small, the wind stress is approximately equal to the vertical integration of four (time derivative, Coriolis, nonlinear, and pressure gradient) terms, as discussed in more detail in section 4. Sanford et al. (2011) estimate the wind stress from the ocean observations by assuming that the wind stress is approximately equal to the integral of the two linear terms (time derivative and Coriolis terms) in the momentum equation (i.e., the nonlinear and pressure gradient terms are negligible). Their investigation reports a relatively low C_d around 1.5×10^{-3} for 10-m wind speed $U_{10} > 25$ m s^{-1}.

Hsu et al. (2017) have significantly improved this approach of wind stress estimation. They first estimate the wind stress from the two linear terms as in Sanford et al. (2011), using ocean current velocity profiles from three electromagnetic autonomous profiling explorer (EM-APEX) floats deployed under Typhoon Megi during the 2010 ITOP (Impact of Typhoons on the Ocean in the Pacific) program (D'Asaro 2014). They restrict their wind stress estimation to the right-front and left-front quadrants of the storm (i.e., prior to arrival of the storm center), where the nonlinear and pressure gradient terms are relatively small. Next, they estimate the contributions from these two terms (neglected in the initial estimates) by running the Price–Pinkel–Weller 3D (PWP3D) ocean model (Price et al. 1986), and correct the wind stress estimates. Finally, the drag coefficient is estimated using the wind speed field that has been carefully constrained by interpolating two wind field snapshots that are generated using stepped frequency microwave radiometer (SFMR) surveys and dropsonde measurements, also performed during the ITOP program. Their final estimates are in the range of roughly 2×10^{-3} to 3.5×10^{-3}, which are much higher than the earlier estimates by Sanford et al. (2011) and more consistent with other studies.

In their subsequent study (Hsu et al. 2019), they estimate C_d in front of five tropical cyclones (Typhoons Megi and Fanapi and Hurricanes Frances, Gustav, and Ike) by using the same approach as in Hsu et al. (2017), using the EM-APEX observations performed during the 2004 CBLAST (Coupled Boundary Layer Air–Sea Transfer) program (Black et al. 2007) and the ITOP program. They report significant storm-dependent variations of the drag coefficient, roughly ranging from 1×10^{-3} to 3.5×10^{-3}. They also suggest that C_d is strongly dependent on a new parameter "effective wind duration," which is a function of U_{10}, storm translation speed, and position relative to the storm center. They find that the faster the storm moves, the larger C_d is, and suggest that the dependence they find may be due to variations in the wave age and wave breaking frequencies under different regimes.

In this study, we estimate the wind stress (drag coefficient) by combining the same ocean current observations under the five TCs (Hsu et al. 2019) and a coupled wave–ocean model. We generate the wind fields in a different manner (see section 2a), and estimate the wind stress by directly comparing the observed ocean currents and simulated ocean currents using the coupled model. The three main objectives of this study are 1) to clarify the effect of wind speed differences among different wind products on C_d estimates under TCs, 2) to carefully examine and correct for the contributions from the nonlinear and pressure gradient terms in the wind stress estimates using the model simulations, and 3) to perform a comprehensive analysis of the sea state dependence of wind stress and drag coefficient. We also examine in detail various surface wave impacts on the upper ocean currents and wind stress estimates.

2. Wind and float observations

a. Wind forcing

Running the coupled wave–ocean model requires a continuous wind field covering the entire model domain over a time period of about 5 days. Therefore, we may not use the same approach of wind field generation by Hsu et al. (2019), relying on wind surveys that are limited in space/time. Instead, a continuous wind field is formed using the parametric wind model (Chen et al. 2020; Reichl et al. 2016a,b) based on the postseason reanalysis best-track database produced by U.S. Navy Joint Typhoon Warning Center (JTWC) for typhoons, and by the National Oceanic and Atmospheric Administration/National Hurricane Center (NOAA/NHC) for hurricanes (HURDAT). The best-track data file contains storm position, propagation speed and direction, center and environmental pressure, radius of outermost closed isobar, maximum wind speed ($V_{\max}$), radius of maximum wind ($R_{\max}$), and radii of 18 m s^{-1} (R_{18}) and 26 m s^{-1} (R_{26}) winds in the four quadrants of the storm every 6 h, when available.

In this study we assume that the 10-m wind speed U_{10} is the neutral 10-m wind speed U_{10N}, since the stability effect is small in high-wind conditions $U_{10} > 25$ m s^{-1}.

b. Wind field in typhoons

For Typhoons Megi and Fanapi, a symmetric azimuthal wind field is first generated by the following modified Rankine vortex:

$$V(r) = \begin{cases} V_{\max}\dfrac{r}{R_{\max}} & r < R_{\max} \\ V_{\max}\left(\dfrac{R_{\max}}{r}\right)^{n} & r \geq R_{\max} \end{cases}, \tag{1}$$

where n is an empirical decay parameter. To introduce a radial wind component and asymmetry to the wind field, the inflow angle (increasing from 0° to 21° with increasing distance from the storm center) is specified and 70% of the storm translation speed is added to the wind field as in Moon et al. (2003). In the western Pacific, there are fewer in situ observations available than in North Atlantic. The best-track

Brought to you by NOAA Central Library | Unauthenticated | Downloaded 10/06/22 12:39 PM UTC

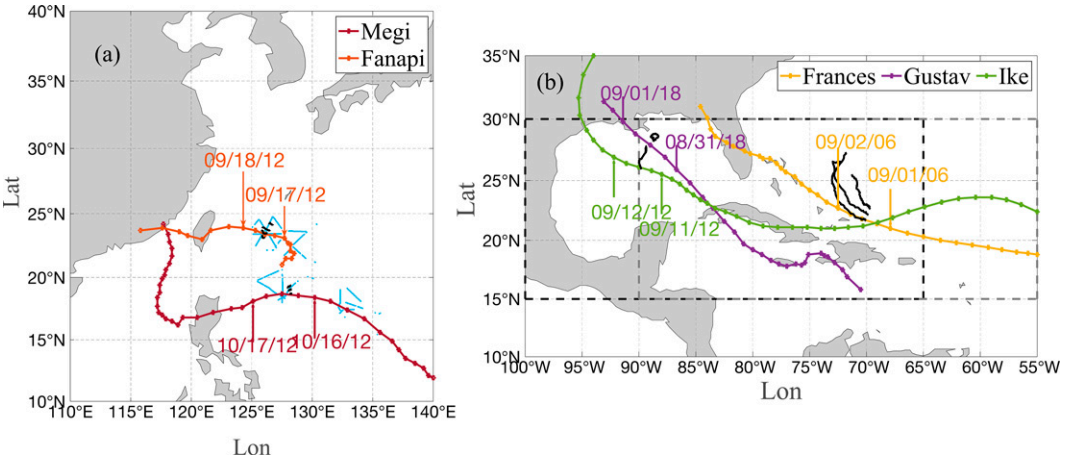

FIG. 1. (a) Tracks of Typhoons Megi (red) and Fanape (dark orange) in the western Pacific. (b) Tracks of Hurricanes Frances (yellow), Gustav (purple), and Ike (green) in the North Atlantic and Gulf of Mexico. In both panels colored dots along the tracks show locations every 6 h, and labels show time (as month/day/hour) 12 h before and after the storm center was closest to the EM-APEX floats. Black lines indicate the trajectory of EM-APEX floats. Blue dotted lines in (a) indicate SFMR surveys with $U_{10} \geq 25$ m s^{-1}. The spatial domain of MOM6–WW3 for typhoons is the area shown in (a). The spatial domain for Hurricane Frances is the gray dashed box in (b). The spatial domain for Hurricanes Gustav and Ike is the black dashed box in (b).

parameters from JTWC are generated mostly based on satellite measurements and are not as accurate as those in North Atlantic where in situ observations are routinely available. Therefore, for both typhoons, V_{max} and R_{max} are adjusted from those in the best-track database. Specifically, we first empirically determine the three parameters (V_{max}, R_{max}, and n) when the SFMR survey is available (three surveys for Megi and two surveys for Fanapi) by minimizing the root-mean-square error (RMSE) between the parametric wind speed U_{10} and the observed SFMR wind speed U_{10} when $U_{10} > 25$ m s^{-1}.

Figure 1 shows the SFMR survey locations. (The third survey of Megi is not shown since it does not impact our drag coefficient estimates.) The SFMR wind speeds have been corrected using the dropsonde measurements as discussed in Hsu et al. (2017), before they are used for adjusting V_{max} and R_{max}. Once V_{max} and R_{max} are determined, we then calculate the bias correction factor c_V (or c_R), which is the ratio of the empirically determined V_{max} (or R_{max}) relative to the V_{max} (or R_{max}) in the best-track database. In between the surveys the three parameters (c_V, c_R, and n) are interpolated. Before the first survey and after the last survey these parameters are set constant. The time series of V_{max} and R_{max} (both before and after the adjustment) as well as n are shown in Fig. 2. The adjusted V_{max} of Megi and Fanapi increase to 86 and 63 m s^{-1} from 80 and 54 m s^{-1}, respectively, and R_{max} decreases to 15 and 22 km from 19 and 28 km, respectively. Figure 3 compares the range of parametric model wind speeds (blue area) and the SFMR wind speeds (black dots), both of them plotted against radius (distance from the storm center), during each survey period. The adjusted parametric wind profiles generally agree well with the SFMR winds. (Note that the parametric wind radial profile varies in time and also depends on the direction relative to the storm propagation direction.)

Figure 4 compares all the SFMR wind speed observations and the corresponding parametric model wind speeds (evaluated at the same time and at the same location). Again, they generally agree well, with the RMSE of 5.8 m s^{-1} for Megi and 4.6 m s^{-1} for Fanapi. The high wind observations of Fanapi are overestimated by the parametric model. This is likely because the wind speed spatial distribution of the model is strongly constrained and cannot always be matched with observations. The model requires that the maximum wind speed occurs to the right of the storm track (which is statistically true in real storms), but the maximum wind region was observed in front of the storm during the SFMR surveys of Fanapi. Nevertheless, the mean biases between the parametric wind and the SFMR wind for Megi and Fanapi are 1.77 and 1.93 m s^{-1}, respectively. This bias is well within the expected uncertainty of SFMR observation (Hsu et al. 2017).

Since the parametric wind model does not provide the background wind field away from the storm, the 10-m wind speed field from the Japanese Meteorological Society Reanalysis product (JRA55; Tsujino et al. 2018) is combined with the parametric wind field. Specifically, the parametric wind is replaced by the JRA55 wind when the latter is larger than the former.

c. *Wind field in hurricanes*

For Atlantic hurricanes the best-track data are more reliable because they are produced by combining many observations including satellite measurements, aircraft surveys, and other in situ observations. Therefore, they can be used without corrections. Furthermore, they provide reliable estimates of radii of 26 and 18 m s^{-1} (R_{26} and R_{18}). When the modified Rankine vortex model is fitted to these parameters, it tends to overestimate the wind speed away from the storm center (Fig. 5). We therefore generate the symmetric azimuthal wind field by combing a Rankine vortex and a vortex with exponential decay:

Brought to you by NOAA Central Library | Unauthenticated | Downloaded 10/06/22 12:39 PM UTC

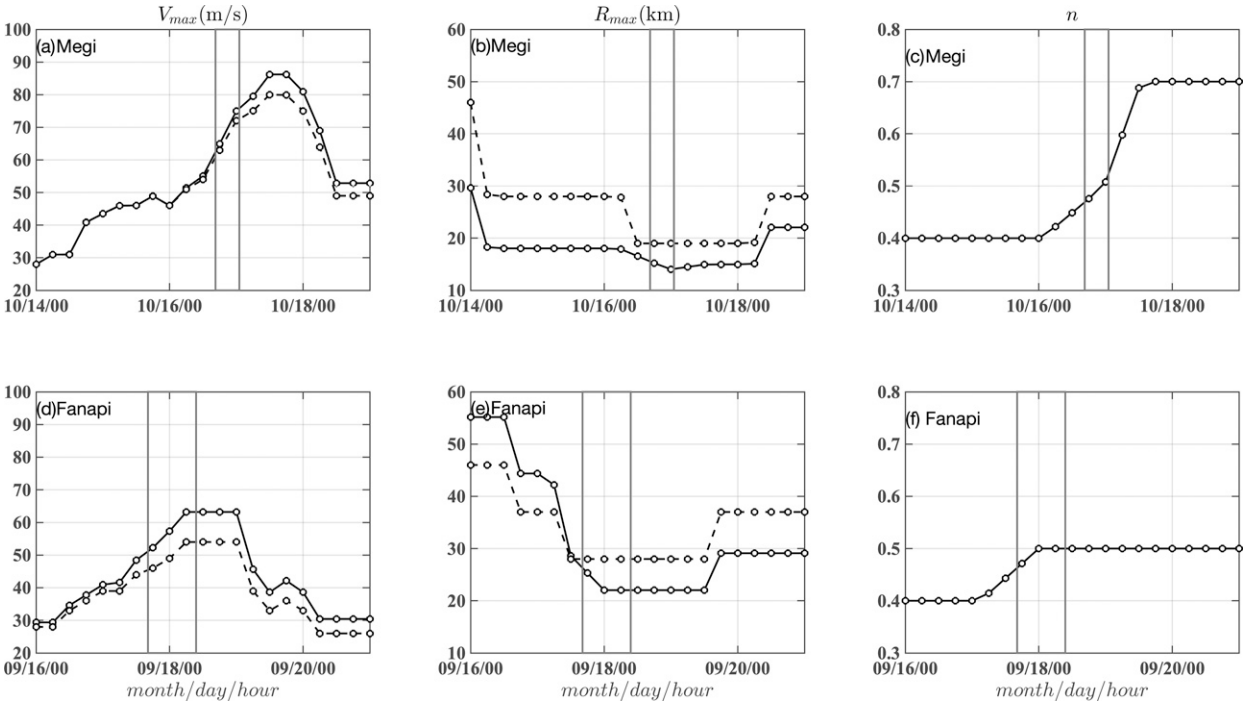

FIG. 2. Time series of retuned (solid line) and original (dashed line) (a),(d) maximum wind speed and (b),(e) radius of maximum wind, as well as (c),(f) empirically determined decay parameter n for Typhoons (top) Megi and (bottom) Fanapi every 6 h. Two vertical gray lines indicate the time period of C_d estimation in this study.

$$V(r) = \begin{cases} V_{\max}\dfrac{r}{R_{\max}} & r < R_{\max} \\ V_{\max}\left(\dfrac{R_{\max}}{r}\right)^{n} & R_{\max} \le r < R_{22} \\ V_{\max}\left(\dfrac{V_{22}}{V_{\max}}\right)^{\frac{R_{\max}-r}{R_{\max}-R_{22}}} & R_{22} \le r \end{cases}, \tag{2}$$

where $V_{22} = 22$ m s^{-1}, $R_{22} = (\overline{R_{18}} + \overline{R_{26}})/2$, and $(\overline{R_{18}}, \overline{R_{26}})$ are the averages of (R_{18}, R_{26}) in four quadrants. The decay parameter n is set so that $V = V_{22}$ at $r = R_{22}$. The time series of $V_{\max}$, $R_{\max}$, $\overline{R_{18}}$ and $\overline{R_{26}}$ for Hurricanes Frances, Gustav, and Ike are shown in Fig. 6. As before, the inflow angle and 70% of the translation speed are added to the wind field and the JRA55 $\mathbf{U}_{10}$ is used for the background wind.

d. *Comparison with observations and with wind field by Hsu et al. (2019)*

The top panels of Fig. 7 shows examples of the two-dimensional wind fields generated by combining the parametric wind model and JRA55 wind [hereafter URI (University of Rhode Island) wind] for five TCs. The timing of each panel has been chosen to be during our wind stress estimation period. They can be compared with the wind fields used by Hsu et al. (2019) [hereafter APL (Applied Physics Laboratory) wind], which has been generated by interpolating the wind maps generated by the SFMR wind surveys. There are significant differences in the spatial patterns of wind speed. Notice, in particular, that the URI wind field is generally broader and more symmetric and the largest wind speed always appears to the right of the storm track, while the APL wind fields are more complex. Since it is not immediately clear which wind products are more accurate, we will use both wind fields in section 5a to investigate the effect of different wind products on the drag coefficient estimates.

During the passage of Frances and Gustav, the National Data Buoy Center (NDBC) buoys (see left panel in Fig. 8) captured the wind field, which can be compared with the URI and APL wind fields. Since the anemometer height varies from 3.6 to 5 m at these NDBC buoys, the 10-m wind speed is calculated by assuming a logarithmic profile (Shearman and Zelenko 1989). The SFMR surveys and best-track message files are both based on 1-min-averaged winds while NDBC buoys report 10-min-averaged winds. Therefore, a gust factor 0.87 is applied to convert the URI and APL winds to the 10-min-averaged winds for comparison (Harper et al. 2010).

Figures 8a and 8b compare the URI wind and observed wind under Frances and Gustav, respectively. Figure 8c compares the APL wind and observed wind under Gustav. (Note that APL wind fields are available only between SFMR surveys.) Generally, both URI wind and APL wind are in good agreement with the NDBC buoy observations except for the low wind speed range. In this study wind stress estimation is performed only at high wind speeds ($U_{10} > 25$ m s^{-1}). Unfortunately, there are not enough measurements during such high wind speeds from the NDBC buoy observations to validate the wind models.

e. *EM-APEX float observation*

In this study observations from 12 EM-APEX floats deployed under five TCs are used, including three floats under

Brought to you by NOAA Central Library | Unauthenticated | Downloaded 10/06/22 12:39 PM UTC

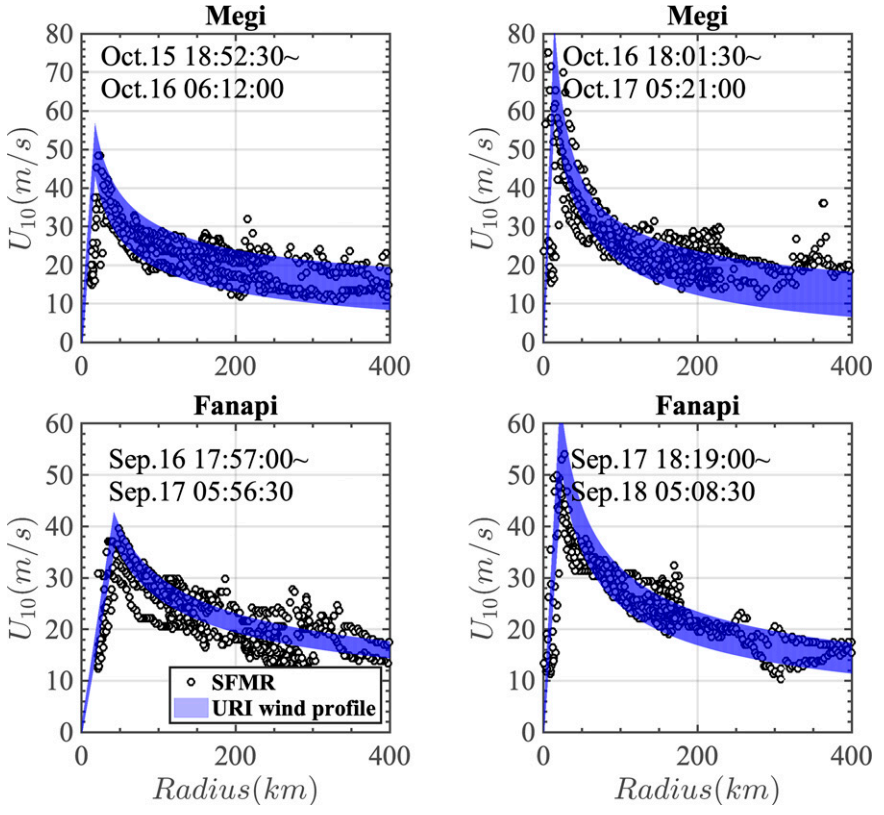

FIG. 3. Comparison of SFMR observed U_{10} (black dots) and URI wind profile (blue envelope) for each SFMR survey under Typhoons (top) Megi and (bottom) Fanapi. The time range (month.day hour:minute:second in 2010) of each survey is labeled in each panel.

Typhoon Megi, four floats under Typhoon Fanapi, three floats under Hurricane Frances, and two floats under Hurricane Gustav (Table 1 and Fig. 1). One float (float 3766) deployed on the left side of Gustav's track drifted to the right side of Ike's track and provided the measurements under Ike as well (Figs. 1 and 7). These EM-APEX float observations provide the vertical profiles of horizontal current, temperature, and salinity roughly every 30 min (Sanford et al. 2011; Hsu et al.

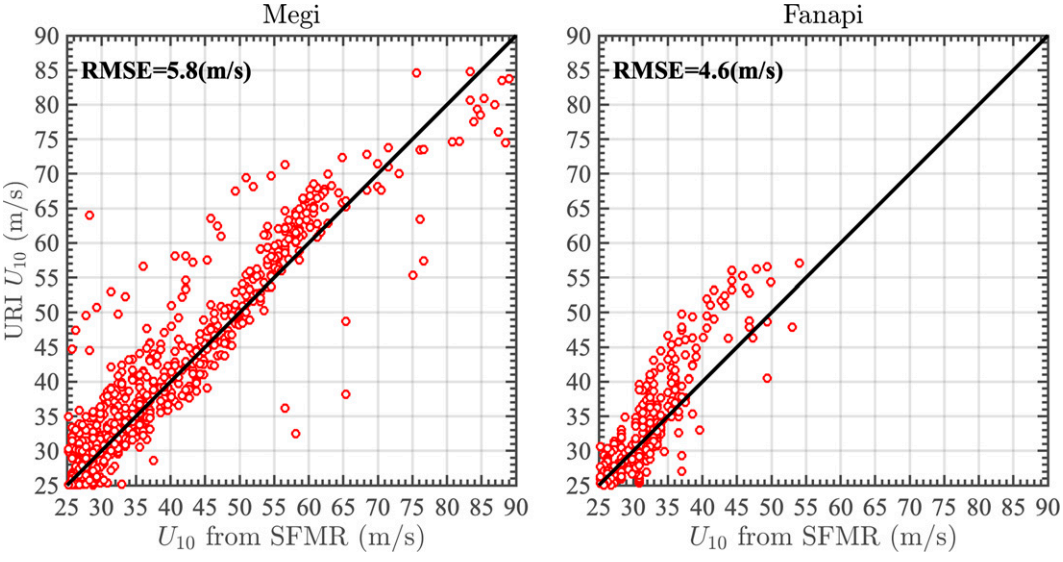

FIG. 4. Comparison of URI U_{10} and SFMR observed U_{10} for all SFMR surveys under Typhoons (left) Megi and (right) Fanapi.

Brought to you by NOAA Central Library | Unauthenticated | Downloaded 10/06/22 12:39 PM UTC

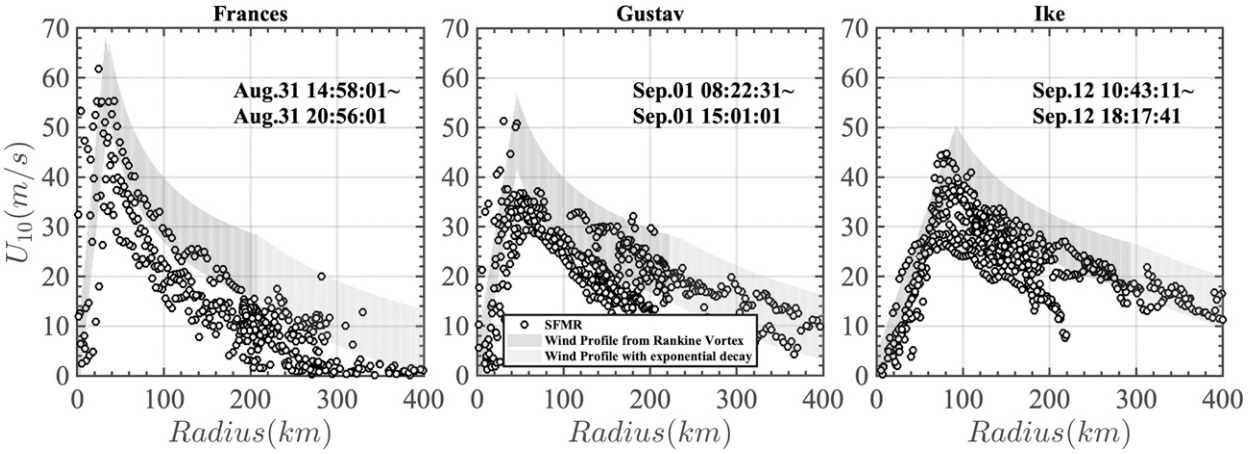

FIG. 5. Comparison of SFMR observed U_{10} (black dots) and URI wind profile that combines the modified Rankine vortex model (dark gray envelope) and a vortex with exponential decay (light gray envelope), under (left) Hurricane Frances, (center) Hurricane Gustav, and (right) Hurricane Ike. The time range (month.day hour:minute:second) of SMFR survey is labeled in each panel.

2017, 2019). The deployment time of each EM-APEX float was about 1 day before the storm arrival (Table 1). The detailed trajectory of 12 EM-APEX floats under TCs are shown in Fig. 7.

As discussed by Hsu et al. (2017, 2019), the measured ocean currents include wind driven currents as well as tidal currents and low-frequency background currents. Since we estimate the wind stress by comparing the observed currents to model simulated currents that are purely wind driven, both the tidal currents and background currents are removed from the measured currents. The full description of extracting wind driven current velocity from the direct EM-APEX velocity measurements is given in Hsu et al. (2017, 2019). Following Hsu et al. (2017, 2019), missing measurements in the upper 30 m under Megi and Frances are filled with the uppermost velocity measurements.

3. Coupled wave–ocean model

The coupled Modular Ocean Model 6–WAVEWATCH III (MOM6-WW3) model is used in this study to simulate the coupled wave–ocean system under TC winds. The MOM6 is

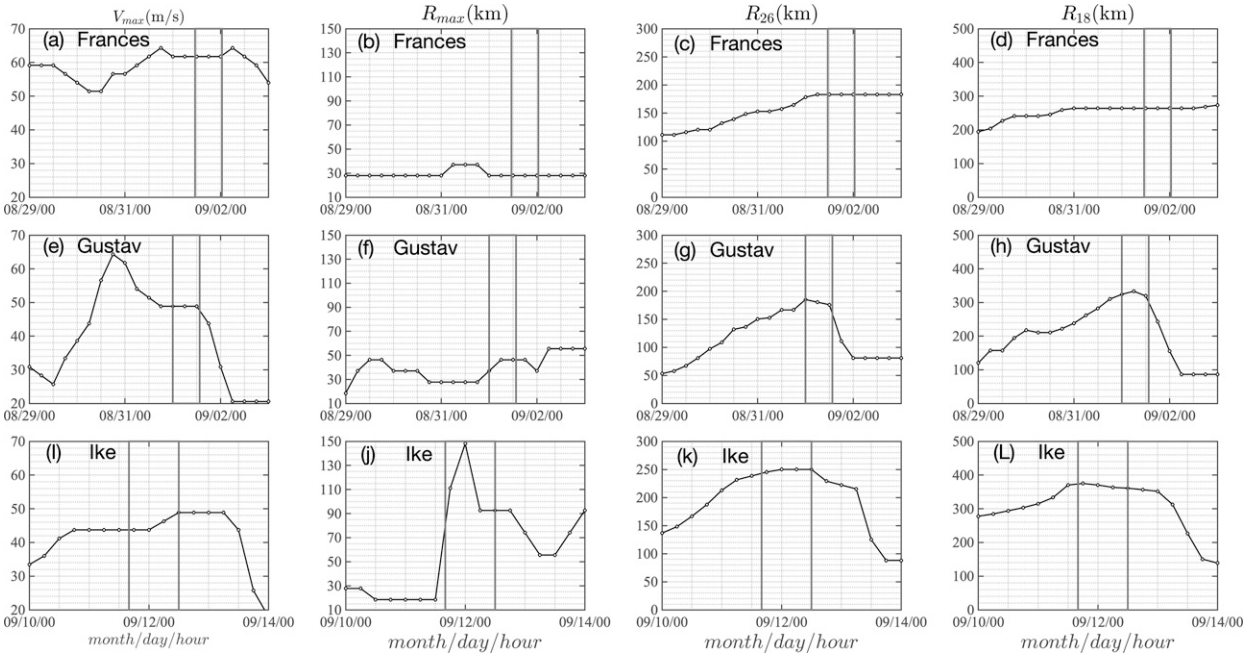

FIG. 6. Time series of (left) maximum wind speed, (middle left) radius of maximum wind, and radii of (middle right) 26 and (right) 18 m s^{-1} wind speeds for Hurricanes (top) Frances, (middle) Gustav, and (bottom) Ike every 6 h. Two vertical gray lines indicate the time period of C_d estimation in this study.

Brought to you by NOAA Central Library | Unauthenticated | Downloaded 10/06/22 12:39 PM UTC

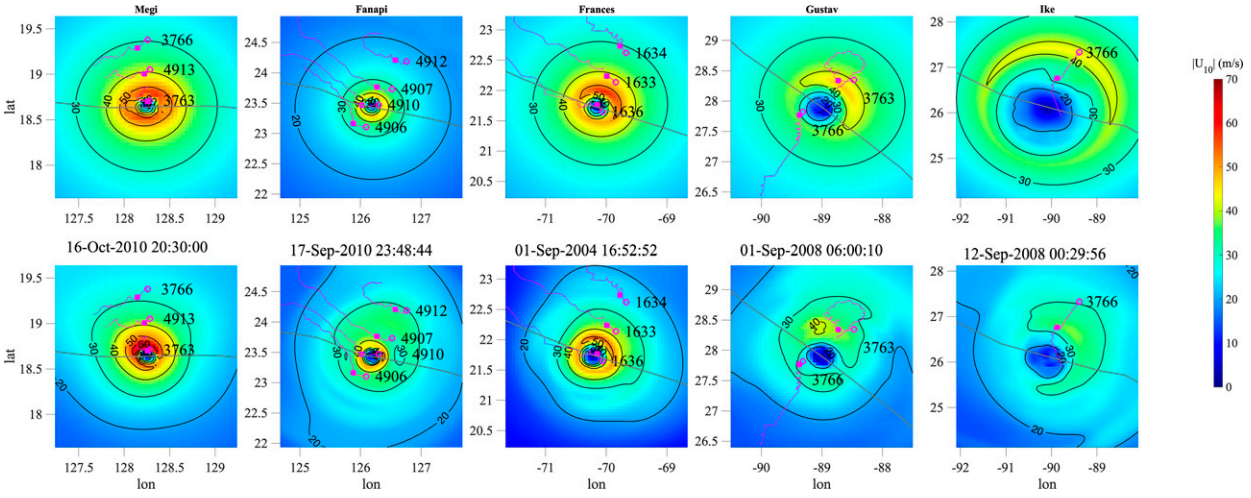

FIG. 7. Comparison of (top) URI wind fields and (bottom) APL wind fields of five tropical cyclones at the time when the storm center was closest to the EM-APEX floats. Gray lines show trajectories of TCs. Purple lines show trajectories of floats. Purple dots mark the initial location of floats. Solid purple squares mark the location of floats at the time of wind map. The name of each EM-APEX float is labeled.

the latest version of the modular ocean model with a hybrid vertical coordinate system developed and maintained by NOAA Geophysical Fluid Dynamics Laboratory (Adcroft et al. 2019). For the wave simulation the WW3 version 6.07 is used (WW3DG 2019). The wind input term (S_{in}) and white-capping terms (S_{dis}) in WW3 in this study are setup following the WW3 ST4 version in Liu et al. (2017) and Chen et al. (2020), which showed good agreement between model results and observations under Hurricane Ivan (see Supporting Information D in the online supplemental material for more details). In the coupled MOM6–WW3 system, the WW3 provides the dominate wavelength and the Stokes drift vector ($\mathbf{u}^S$) to the ocean model. The MOM6 provides the near surface horizontal current vector ($\mathbf{u}^W$) to the WW3. In these simulations we use the K-profile parameterization (KPP) for ocean surface boundary layer mixing

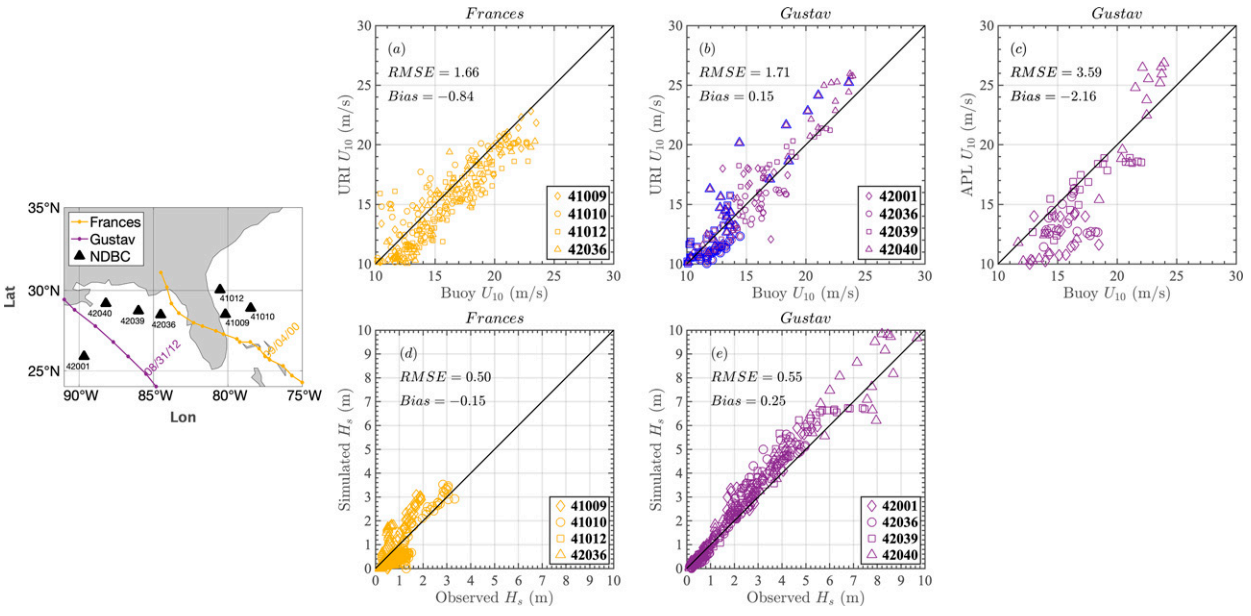

FIG. 8. (left) Locations of NDBC buoys (black triangles) in North Atlantic and Gulf of Mexico and tracks of Frances (yellow dotted curves) and Gustav (purple dotted curves). Comparison of URI U_{10} and buoy observations under (a) Frances and (b) Gustav. (c) Comparison of APL U_{10} and buoy observations under Gustav. Blue symbols in (b) are DATA when APL wind was not available. Comparison of significant wave height (H_s) between simulation and observation under (d) Frances and (e) Gustav. In all panels different symbols indicate different buoys. The root-mean-square error and bias between model simulation and observation are labeled.

Brought to you by NOAA Central Library | Unauthenticated | Downloaded 10/06/22 12:39 PM UTC

TABLE 1. List of 12 EM-APEX floats deployed under five tropical cyclones, including name, location, and time of initial profiling, and arrival time of TC.

Tropical cyclone	EM-APEX float name	Lon (°E)	Lat (°N)	First profiling time	Arrival time of TC
Frances	em1633	−69.8	22.1	1443 UTC 31 Aug 2004	1652 UTC 1 Sep 2004
	em1636	−70.1	21.7	1410 UTC 31 Aug 2004	1650 UTC 1 Sep 2004
	em1634	−69.7	22.6	1450 UTC 31 Aug 2004	1640 UTC 1 Sep 2004
Gustav	em3763	−88.5	28.3	1400 UTC 31 Aug 2008	0600 UTC 1 Sep 2008
	em3766	−89.3	27.8	1404 UTC 31 Aug 2008	0524 UTC 1 Sep 2008
Ike	em3766	−89.3	27.8	1404 UTC 31 Aug 2008	0030 UTC 12 Sep 2008
Fanapi	em4912	126.8	24.2	0221 UTC 17 Sep 2010	2204 UTC 17 Sep 2010
	em4907	126.5	23.7	0232 UTC 17 Sep 2010	2333 UTC 17 Sep 2010
	em4910	126.3	23.5	0316 UTC 17 Sep 2010	0052 UTC 18 Sep 2010
	em4906	126.1	23.1	0241 UTC 17 Sep 2010	0109 UTC 18 Sep 2010
Megi	em3766	128.3	19.4	0035 UTC 16 Oct 2010	2055 UTC 16 Oct 2010
	em4913	128.3	19.1	0052 UTC 16 Oct 2010	2030 UTC 16 Oct 2010
	em3763	128.3	18.7	0059 UTC 16 Oct 2010	2030 UTC 16 Oct 2010

in MOM6 via the public Community Vertical Mixing (CVMix) project.

Three large, deep-water (4000 m) computational domains are used for both the ocean and the wave models. As shown in Fig. 1, the domain in the western Pacific for Megi and Fanapi is 10°–40°N, 110°–140°E. The domain in the North Atlantic for Frances is 15°–30°N, 90°–55°W. In Gulf of Mexico, the domain for both Gustav and Ike is 15°–30°N, 100°–65°W. The spatial resolution is 1/24°, which is around 4.5 km, and the temporal resolution is 300 s for both MOM6 and WW3. We note that it is important to use a spatial resolution of 1/24° or higher for WW3, since Chen et al. (2018) found that a coarser spatial resolution of WW3 may introduce a significant bias of wave spectra under TCs. The vertical resolution in MOM6 is 2 m in the upper ocean (50 m), increases linearly to 10 m at a 100-m depth and gradually increases below. The vertical coordinate in MOM6 is set to the stretched geopotential, or Z^* mode for these experiments. The surface wave spectrum in WW3 is discretized using 48 directions and 40 relative frequencies. The initial temperature and salinity profiles in the model experiments are prescribed spatially homogeneous, and are determined by spatially and temporally averaging the vertical profiles from EM-APEX floats observations before the arrival of TC's eye, when JRA55 U_{10} is larger than the parametric U_{10}.

Since our later investigation of the sea state dependence of drag coefficient (section 6) relies on the WW3 simulation results, it is important to clarify their accuracy. The wave parameters we will later utilize include misalignment angle ψ between wind and dominant (or peak) waves, wave age c_p/u_*, and wave steepness H_s/L_p, in conditions of dominant wavelength from 129 to 384 m and H_s from 6.5 to 15 m. Therefore, WW3 predictions of the dominant wave direction, dominant wavelength, and significant wave height need to be sufficiently accurate in such conditions. In three previous studies (Moon et al. 2003; Fan et al. 2009; Liu et al. 2017) WW3 predictions of these wave parameters under TCs were carefully validated against National Aeronautics and Space Administration (NASA) Scanning Radar Altimeter (SRA) measurements. The accuracy of wave observations of SRA has been well established (Walsh et al. 1985, 1987, 1989). In the 1990s, the SRA mode of the NASA 36-GHz multimode airborne radar altimeter was developed for installation on NOAA research aircraft that were flying missions into tropical cyclones (PopStefanija et al. 2021). The detailed data processing of SRA measurements are well documented in Walsh et al. (2002) and Wright et al. (2001). In particular, SRA observations of dominant wavelength and direction are highly reliable provided the dominant waves are longer than 100 m (E. Walsh 2022, personal communication).

Moon et al. (2003) conducted detailed comparison of wave spectra from WW3 with SRA observation under Hurricane Bonnie (1998). Their Fig. 13 (reproduced in the supplemental material, Supporting Information A) shows excellent agreement of dominant wavelength, dominant wave direction and significant wave height along all SRA tracks in open ocean, except for one SRA track near the landfalling storm. Using SRA measurements under Hurricane Ivan (2004), Fan et al. (2009) also show excellent agreement of dominant wavelength, dominant wave direction and significant wave height along SRA tracks in their Fig. 4 (reproduced in the supplemental material, Supporting Information A). In particular, they show that the agreement of significant wave height improves when ocean surface currents are included in the WW3 simulation. The coupled wave–ocean model in this study also includes the ocean current effect on wave simulations. Fan et al. (2009) also show good agreement of significant wave height (above ~6 m) between SRA measurements and satellite measurements from *Envisat* and *ERS-2*. More recently, Liu et al. (2017) investigated WW3 performance under Hurricane Ivan (2004) by comparing WW3 with updated source terms with SRA observations. Their Fig. 5 clearly

Brought to you by NOAA Central Library | Unauthenticated | Downloaded 10/06/22 12:39 PM UTC

confirms excellent agreement of significant wave height, mean wave direction, and mean wave period.

Based on the comparison between WW3 simulations and SRA measurements in these three studies (Moon et al. 2003; Fan et al. 2009; Liu et al. 2017), we may estimate the WW3 uncertainty of dominant wave direction to be ~10°. The uncertainty of dominant wavelength is ~50 m, which introduces ~0.1 uncertainty of wave age. For significant wave height above 6 m, its uncertainty of ~1 m introduces ~0.005 uncertainty of wave steepness. These uncertainty estimates are sufficiently small for our later analysis of the sea state dependence of drag coefficient in section 6.

Finally, Figs. 8e and 8d confirm that the WW3 simulations of significant wave height under high-wind condition are consistent with the buoy observations under Hurricane Gustav. The bias between WW3 simulated H_s and NDBC buoy observations are comparable to those in previous studies (Fan et al. 2009; Liu et al. 2017; Moon et al. 2003).

In this study we investigate the impacts of ocean surface waves (sea states) on four different air–sea interaction processes. First, surface waves modify the drag coefficient (or the equivalent surface roughness) mainly because wind stress is mostly determined by form drag of a spectrum of surface waves in higher wind speeds. Second, when surface waves are growing/decaying, the stress applied to the upper ocean may be different from the wind stress (wave-induced momentum flux budget). Third, upper-ocean turbulent mixing is modified by surface waves (Langmuir turbulence). Fourth, upper-ocean currents interact with surface waves through Coriolis–Stokes force, Stokes-shear force, and other processes (Suzuki and Fox-Kemper 2016). While the first wave effect (sea state–dependent drag coefficient) affects both atmosphere and ocean, the other three wave effects only impact the subsurface currents and turbulence.

In this study we thoroughly investigate the first wave effect (sea state dependence of drag coefficient) in section 6. While the other three wave effects do not impact the drag coefficient itself, they may impact our drag coefficient "estimation," because our estimation is made using the upper-ocean current observations. Therefore, a series of numerical experiments are performed to examine the other three surface wave impacts, that is, Langmuir turbulence, the wave-induced momentum flux budget, and wave–current interactions, on the upper-ocean current responses and the wind stress estimation (Table 2). In MOM6 the following Boussinesq momentum equations (given here in geopotential/height coordinates) are solved (Adcroft et al. 2019):

$$\partial_t u_i + (\mathbf{u}\cdot\nabla)u_i + \varepsilon_{i3j} f u_j + \frac{1}{\rho_0}\partial_i p - \frac{1}{\rho_0}\mathcal{F} = 0, \quad i = 1,2; \quad j = 1,2 \tag{3}$$

$$\frac{1}{\rho_0}\partial_z p + \frac{\rho}{\rho_0} g = 0, \tag{4}$$

where $\mathbf{u}$ is the (3D) Eulerian velocity, f is the local Coriolis frequency, ρ_0 is the constant Boussinesq reference density, and ρ is the in situ density. In the horizontal momentum equations $\mathcal{F}$ represents the accelerations due to the divergence of stresses. In this study the horizontal stress is negligible and $\mathcal{F}$ is practically equal to the vertical gradient of the vertical frictional turbulent stress $\partial\tau_i/\partial z$.

The turbulent stress τ_i is parameterized using two different KPP schemes (KPP-iLT and KPP-LT) proposed by Reichl et al. (2016b), who have carefully tuned the KPP schemes against a large number of large-eddy simulation (LES) runs under TCs. The KPP-iLT is a standard KPP model without explicit surface wave impacts, but the critical Richardson number is set $\mathrm{Ri}_{\mathrm{cr}} = 0.35$ so that it is consistent with typical (sea state independent) Langmuir turbulence conditions under TCs. The KPP-LT incorporates explicit sea state–dependent Langmuir turbulence, mainly by setting the eddy viscosity as a function of the turbulent Langmuir number (ratio of the Stokes drift velocity to the friction velocity), and by parameterizing the turbulent mixing in terms of the Lagrangian current shear instead of the Eulerian current shear. Further details of these mixing schemes are given in Reichl et al. (2016b).

As shown in Table 2, Experiment A is performed with the implicit (sea state independent) Langmuir turbulence KPP model (KPP-iLT), while Experiment B is performed with the explicit (sea state dependent) Langmuir turbulence KPP model (KPP-LT). Experiment C is carried out to study the influence of the air–sea momentum flux budget, that is, the difference between the momentum flux from atmosphere (wind stress) and the momentum flux into upper ocean, due to growing/decaying surface waves. In this experiment the surface forcing for the upper ocean is modified from the wind stress by $\Delta\tau_i^{\mathrm{bg}}$ (Fan et al. 2009, 2010; Smith 2006):

$$\Delta\tau_i^{\mathrm{bg}} = \rho_0\left[-\partial_t M_i - \partial_j S_{ij} - \partial_j\left(M_i u_j^w\right) - M_j\partial_i u_j^w\right]. \tag{5}$$

Here, $M_i = \int_{-\infty}^{0} u_i^S(z)dz$ is the vertically integrated Stokes drift, S_{ij} is the radiation stress, and u_i^w is the near surface current (Smith 2006). Fan et al. (2010) investigated the air–sea momentum flux budget by calculating the first two terms on the right of Eq. (5) since the last two terms are much smaller–roughly by the ratio of the surface current and the group velocity of dominant waves. Nevertheless, these smaller terms are retained in this study because they are comparable to the horizontal Stokes shear force discussed below. The mixing scheme in Experiment C is KPP-LT.

Experiment D includes the wave–current interaction effects in addition to the KPP-LT and the air–sea momentum flux budget, that is, includes all the wave impacts addressed in this study. Namely, the governing equation for the ocean currents are modified to

$$\partial_t u_i + (\mathbf{u}^L\cdot\nabla)u_i + \varepsilon_{i3j} f u_j^L + \frac{1}{\rho_0}\partial_i p - \frac{1}{\rho_0}\mathcal{F} = -u_j^L\partial_i u_j^S \tag{6}$$

$$\frac{1}{\rho_0}\partial_z p + \frac{\rho}{\rho_0} g = -u_j^L\partial_z u_j^S, \tag{7}$$

Brought to you by NOAA Central Library | Unauthenticated | Downloaded 10/06/22 12:39 PM UTC

TABLE 2. List of experiments with MOM6–WW3.

Expt	Mixing scheme	Surface forcing	Sea state Langmuir turbulence	Air–sea momentum flux budget	Wave–current interaction
A	KPP-iLT	τ_{wind}	No	No	No
B	KPP-LT	τ_{wind}	Yes	No	No
C	KPP-LT	$\tau_{\text{wind}} + \tau^{\text{bg}}$	Yes	Yes	No
D	KPP-LT	$\tau_{\text{wind}} + \tau^{\text{bg}} + \tau^{\text{wc}}$, ΔP^{wc}	Yes	Yes	Yes

which include three surface wave effects (Suzuki and Fox-Kemper 2016). Namely, 1) the advection is by the Lagrangian current ($\mathbf{u}^L = \mathbf{u} + \mathbf{u}^S$) instead of by the Eulerian current [second term in Eq. (6)], 2) the Coriolis force applies to the Lagrangian current instead of the Eulerian current [Coriolis–Stokes force, third term in Eq. (6)], and 3) the Stokes shear force applies [right-hand side terms in Eq. (6) and (7)]. The continuity equation is also rewritten in terms of Lagrangian current instead of Eulerian current.

In principle, the MOM6 code needs to be modified to properly solve these equations. However, in this study we take a simpler (but less accurate) approach. First, Eq. (6) is rewritten in terms of the Lagrangian current:

$$\partial_t u_i^L + (\mathbf{u}^L \cdot \nabla) u_i^L + \varepsilon_{i3j} f u_j^L + \frac{1}{\rho_0}\partial_i p - \frac{1}{\rho_0}\mathcal{F} = (\mathbf{u}^L \cdot \nabla) u_i^S - u_j^L \partial_i u_j^S + \partial_t u_i^S. \tag{8}$$

Then, the left terms of Eqs. (8) and (7) are identical to the momentum equations solved in MOM6 [Eqs. (3) and (4)], if the MOM6 solves for the Lagrangian current $\mathbf{u}^L$ instead of the Eulerian current $\mathbf{u}$, and $\mathcal{F}$ is also parameterized using $\mathbf{u}^L$. For the horizontal momentum equation [Eq. (8)] only the three extra terms on the right need to be added as extra forcing. Since the Stokes drift decays with depth rather quickly, these terms only apply to the shallow upper layer. We therefore assume that these three forcing terms apply at the surface instead of in the interior. Specifically, if we integrate Eq. (8) from depth $-H_s$ to the sea surface, where H_s is the depth of the Stokes layer (where the Stokes drift is significant),

$$\rho_0 \int_{-H_s}^{0} \left[\partial_t u_i^L + (\mathbf{u}^L \cdot \nabla) u_i^L + \varepsilon_{i3j} f u_j^L + \frac{1}{\rho_0}\partial_i p\right] dz = \rho_0 \int_{-H_s}^{0} \left[(\mathbf{u}^L \cdot \nabla) u_i^S dz - u_j^L \partial_i u_j^S dz + \partial_t u_i^S dz\right] + \tau_{i_{z=0}} - \tau_{i_{z=-H_s}}. \tag{9}$$

The first term (integral of three terms) on the right of Eq. (9) is denoted as $\Delta\tau_i^{\text{wc}}$ and treated as a modification to the wind stress. The vertical momentum equation, Eq. (4), is also modified by the vertical Stokes shear force as shown in Eq. (7). The vertically integrated Eq. (7) becomes

$$p_{z=-H_s} = p_{z=0} + \int_{-H_s}^{0} \rho g dz + \rho_0 \int_{-H_s}^{0} u_j^L \partial_z u_j^S dz, \tag{10}$$

that is, the pressure field below the Stokes layer is modified as if the surface atmospheric pressure is modified by the last term on the right of Eq. (10), which is named Δp^{wc}. This surface pressure correction term Δp^{wc} is also introduce into Experiment D. Although our approach does not accurately resolve the surface wave impact inside the Stokes layer, we consider this as a reasonable approach (as a first step) to perform a sensitivity study of the wave–current interaction effects.

4. Estimation of drag coefficient

In this section we describe how we estimate the wind stress by combining the observation and the model.

a. *Uncorrected drag coefficient*

As discussed by Sanford et al. (2011) and Hsu et al. (2017, 2019), the depth-integrated horizontal momentum equation from the sea surface to a depth $-H$ becomes

$$\rho_0 \int_{-H}^{0} \left[\partial_t u_i + (\mathbf{u} \cdot \nabla) u_i + \varepsilon_{i3j} f u_j + \frac{1}{\rho_0}\partial_i p\right] dz = \tau_{i_{z=0}} - \tau_{i_{z=-H}}. \tag{11}$$

Here, $\tau_{iz=0}$ and $\tau_{iz=-H}$ are the surface wind stress (or the modified stress if the surface wave effects are included) and the stress at $z = -H$. If we choose a sufficiently deep $-H$ so that the stress is negligible there, the wind stress is equal to the vertical integral of four terms on the left hand side of Eq. (11). In this study we choose $H = 100$ m as in Hsu et al. (2019). Hsu et al. (2017, 2019) first estimate the wind stress by integrating the two linear terms ($\partial_t u_i + \varepsilon_{i3j} f u_j$) using the EM-APEX ocean current observations. Since the nonlinear and pressure gradient terms cannot be obtained from the observational data, they use model-simulated nonlinear and pressure gradient terms to estimate their contribution to the stress calculation, and restrict their wind stress estimation to the front of TCs, where these terms are small.

In Hsu et al. (2017, 2019) the wind stress is estimated for each EM-APEX profile, but the time derivative $\partial_t u_i$ is estimated from two profiles (one before and one after) that are Δt apart. Since the float drifts over that time period, the measurements actually provide $\Delta u_i/\Delta t$, where Δu_i is the difference of the observed horizontal current (including the float advection effect), and it is different from $\partial_t u_i$. We investigate the difference between $\Delta u_i/\Delta t$ and $\partial_t u_i$ in section 5.

Following Hsu et al. (2017, 2019), we first estimate the wind stress $\boldsymbol{\sigma}^{\text{obs}} = (\sigma_x^{\text{obs}}, \sigma_y^{\text{obs}})$ directly from the wind-driven current observations without correcting for the nonlinear and pressure gradient terms:

Brought to you by NOAA Central Library | Unauthenticated | Downloaded 10/06/22 12:39 PM UTC

$$\sigma_x^{\text{obs}} = \rho_0 \int_{-H}^{0} (\Delta u_{\text{obs}}/\Delta t - f v_{\text{obs}}) dz,$$
$$\sigma_y^{\text{obs}} = \rho_0 \int_{-H}^{0} (\Delta v_{\text{obs}}/\Delta t + f u_{\text{obs}}) dz, \quad (12)$$

where $\mathbf{u}_{\text{obs}} = (u_{\text{obs}}, v_{\text{obs}})$ is the wind induced current from the EM-APEX floats. (Here, $\boldsymbol{\sigma}$ denotes the uncorrected wind stress estimates and is distinguished from the corrected wind stress $\boldsymbol{\tau}$.) The drag coefficient C_d^* and the misalignment angle ϕ^* between the wind stress and the wind speed (positive ϕ^* means wind stress direction to the left of wind speed direction) can be estimated as

$$C_d^* = \frac{|\boldsymbol{\sigma}^{\text{obs}}|}{\rho_{\text{air}} |U_{10}|^2}, \quad (13)$$

$$\phi^* = \tan^{-1} \frac{\sigma_y^{\text{obs}}}{\sigma_x^{\text{obs}}} - \tan^{-1}\left(\frac{v_{10}}{u_{10}}\right). \quad (14)$$

Here, (u_{10}, v_{10}) are the zonal and meridional components of $\mathbf{U}_{10}$, and an asterisk denotes the uncorrected estimates. In section 5a we perform this exercise using both the URI and APL wind fields in front of TCs to investigate the effect of wind speed uncertainty on the (uncorrected) drag coefficient estimates.

b. Corrected drag coefficient

In this study the effects of nonlinear and pressure gradient terms are not introduced as corrections to be added. Instead, we will take the following steps.

1) The coupled MOM6–WW3 model is run using the URI wind field and an assumed (initial guess) drag coefficient (C_d^{init}) as a function of U_{10}.
2) We simulate the (uncorrected) stress calculation from the float observations by using the model simulated current at the same time and at the same location as the float observation. Specifically, we calculate $\boldsymbol{\sigma}^{\text{sim}} = (\sigma_x^{\text{sim}}, \sigma_y^{\text{sim}})$ with

$$\sigma_x^{\text{sim}} = \rho_0 \int_{-H}^{0} (\Delta u_{\text{sim}}/\Delta t - f v_{\text{sim}}) dz,$$
$$\sigma_y^{\text{sim}} = \rho_0 \int_{-H}^{0} (\Delta v_{\text{sim}}/\Delta t + f u_{\text{sim}}) dz \quad (15)$$

for each EM-APEX profile, where $\mathbf{u}_{\text{sim}} = (u_{\text{sim}}, v_{\text{sim}})$ is the simulated current.
3) We compare the magnitude and direction of $\boldsymbol{\sigma}^{\text{obs}}$ and $\boldsymbol{\sigma}^{\text{sim}}$ for each data point (i.e., each EM-APEX profile), including those behind the storm. Specifically, we calculate the magnitude ratio M_r:

$$M_r = \frac{|\boldsymbol{\sigma}^{\text{obs}}|}{|\boldsymbol{\sigma}^{\text{sim}}|} \quad (16)$$

and the misalignment angle ϕ between the simulation and the observation,

$$\phi = \tan^{-1}\left(\frac{\sigma_y^{\text{obs}}}{\sigma_x^{\text{obs}}}\right) - \tan^{-1}\left(\frac{\sigma_y^{\text{sim}}}{\sigma_x^{\text{sim}}}\right). \quad (17)$$

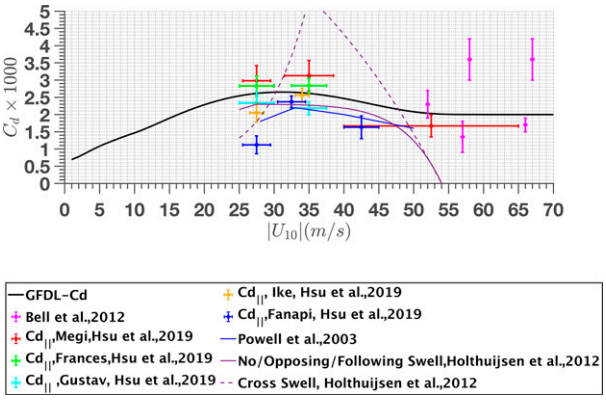

FIG. 9. GFDL C_d as a function of U_{10} (black line) is compared with results from previous studies under TCs.

Assuming that the URI wind fields are reasonably accurate, if the drag coefficient C_d^{init} used in the simulation is correct, we would expect that M_r is close to 1 and ϕ is close to 0 on average. (If not, we need to modify C_d^{init} and repeat the simulations. However, we will find that our initial assumed drag coefficient is sufficiently accurate.) Furthermore, if we assume that $\boldsymbol{\sigma}^{\text{sim}}$ responds linearly to the locally imposed wind stress (i.e., $|\boldsymbol{\sigma}^{\text{sim}}|$ is proportional to the magnitude of the imposed stress, and the direction of $\boldsymbol{\sigma}^{\text{sim}}$ changes in the same manner as the direction of the imposed stress if it is changed), the drag coefficient can be estimated from each observation as

$$C_d = {C_d}^{\text{init}} M_r, \quad (18)$$

ϕ is the estimated misalignment angle between the wind speed and the wind stress, and the downwind drag coefficient is calculated as $C_{d\|} = C_d \cos\phi$ (Hsu et al. 2017). (If ϕ is positive, the wind stress direction is to the left of the wind speed direction.) Then, the friction velocity u_*, the surface roughness z_o, and the Charnock coefficient Z_{ch} are calculated using $u_*^2 = C_d U_{10}^2$, $C_d = \{\kappa/[\ln(z/z_0)]\}^2$ with $z = 10$ m, and $Z_{\text{ch}} = z_o g/u_*^2$.

As an initial estimate of the drag coefficient, we use the drag coefficient implemented in the Geophysical Fluid Dynamics Laboratory (GFDL) hurricane model in 2015 (Ginis et al. 2015) (hereafter GFDL C_d; Fig. 9). This particular C_d parameterization is chosen because it produced the best tropical cyclone intensity forecasts using the GFDL and HWRF hurricane models based on a large number of storm simulations (Ginis et al. 2015; Biswas 2018). It is close to the COARE 3.5 formulation at wind speeds lower than 23 m s^{-1} (Edson et al. 2013) and consistent with the theoretical formulation of Soloviev et al. (2014) above 30 m s^{-1}. Figure 9 shows that the GFDL C_d is close to the average of the previous observations under TCs including the results of Hsu et al. (2019). We find that the model simulation using this drag coefficient is reasonably accurate, i.e., the resulting bin-averaged values of M_r and ϕ are sufficiently close to 1 and 0, respectively. Therefore, we do not modify C_d^{init} and repeat the

Brought to you by NOAA Central Library | Unauthenticated | Downloaded 10/06/22 12:39 PM UTC

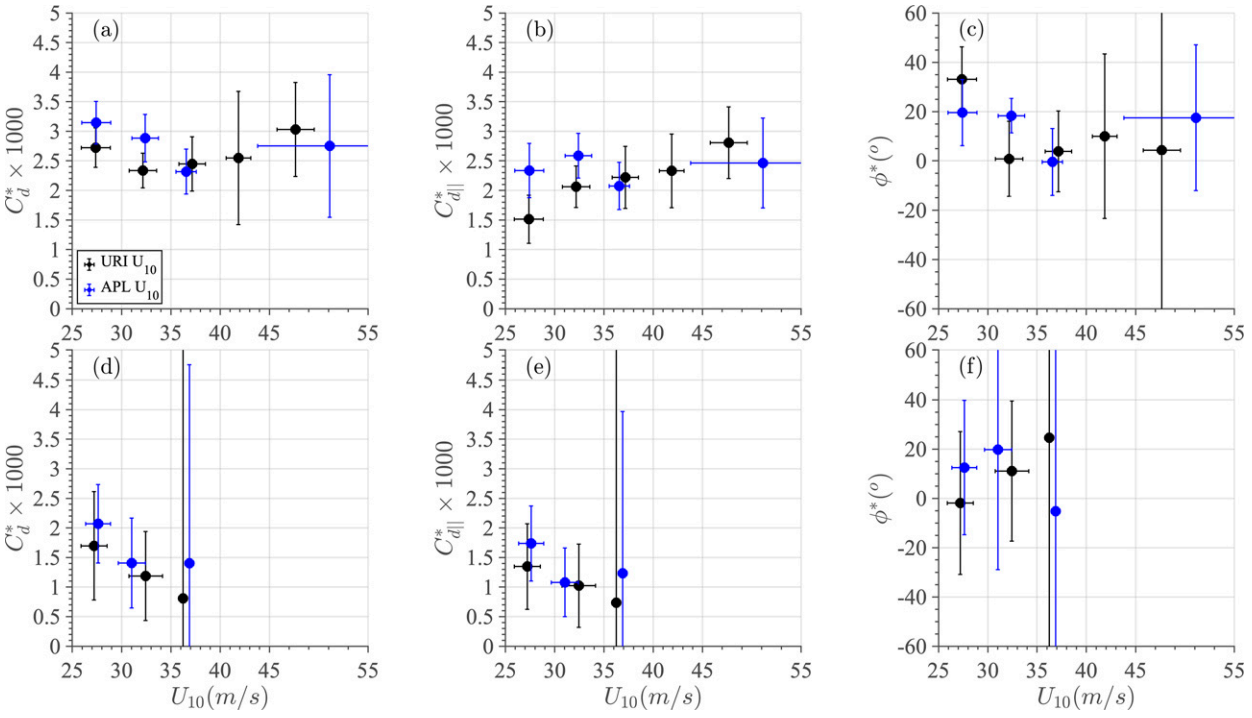

FIG. 10. (a),(d) Bin-averaged drag coefficient C_d^*, (b),(e) along-wind drag coefficient $C_{d\|}^*$, and (c),(f) angle ϕ^* between wind stress and wind speed, estimated using URI wind (black) or APL wind (blue), and using float measurements in (top) front-right and (bottom) front-left sectors of five TCs. The horizontal error bar is the standard deviation of wind speed in each bin. The vertical error bar is the 95% confidence level in each bin.

simulation. However, in one experiment we have estimated C_d based on ocean simulations using a different C_d^{init} (1.2 times GFDL C_d). We have found that the resulting C_d estimates are almost identical to the original estimates, that is, our C_d estimation is not sensitive to the choice of C_d^{init} (see supplemental material, Supporting Information B).

c. *Data quality control process*

Our approach of the drag coefficient estimation described in the previous subsection relies on an assumption that $\boldsymbol{\sigma}^{\text{sim}}$ responds linearly to the locally imposed wind stress, that is, $\boldsymbol{\sigma}^{\text{sim}}$ is close to the imposed wind stress and the contribution from the other terms is reasonably small. Therefore, we carefully examine the validity of this assumption for each observational data point (each EM-APEX profile). Namely,

1) We repeat all the simulations with a drag coefficient that is 20% larger. If the resulting magnitude $|\boldsymbol{\sigma}^{\text{sim}}|$ increases more than 30% or less than 10% for a particular data point, it is excluded from the analysis.
2) If $|\boldsymbol{\sigma}^{\text{sim}}|$ is less than 70% or more than 130% of the imposed wind stress magnitude for a particular data point, it is excluded from the analysis.

Note that these two steps are purely based on the model simulations; we do not impose any conditions on the observational data. After these quality control processes, the number of data samples with $U_{10} \geq 25$ m s^{-1} has decreased from 326 to 195. Nevertheless, we now utilize a significant number of data points behind the storm that were not included in the previous studies.

By repeating the analyses using increased and reduced data samples (with more relaxed and more strict data quality control criteria), we have ascertained that adjusting these criteria do not significantly change the conclusions of this study (see supplemental material, Supporting Information C).

5. Results of drag coefficient

In this section, the results are mostly presented as bin averages for wind bins of 25–30, 30–35, 35–40, 40–45, and >45 m s^{-1} (from Fig. 10). The horizontal error bar is the standard deviation of wind speed in each bin. The vertical error bar is the 95% confidence level in each bin. The 95% confidence level is infinite when there is only one data point within the bin.

a. *Effect of different wind products on drag coefficient estimates*

The accuracy of estimated drag coefficient depends on the accuracy of wind speed products. To investigate the impact of different wind products on drag coefficient estimates, we present C_d^*, $C_{d\|}^* = C_d^* \cos\phi^*$, and ϕ^* with both the URI wind and APL wind in Fig. 10. Note that C_d^*, $C_{d\|}^*$, and ϕ^* are estimated from the integration of linear (measurable) terms only and are not as accurate as the estimates presented later. The

Brought to you by NOAA Central Library | Unauthenticated | Downloaded 10/06/22 12:39 PM UTC

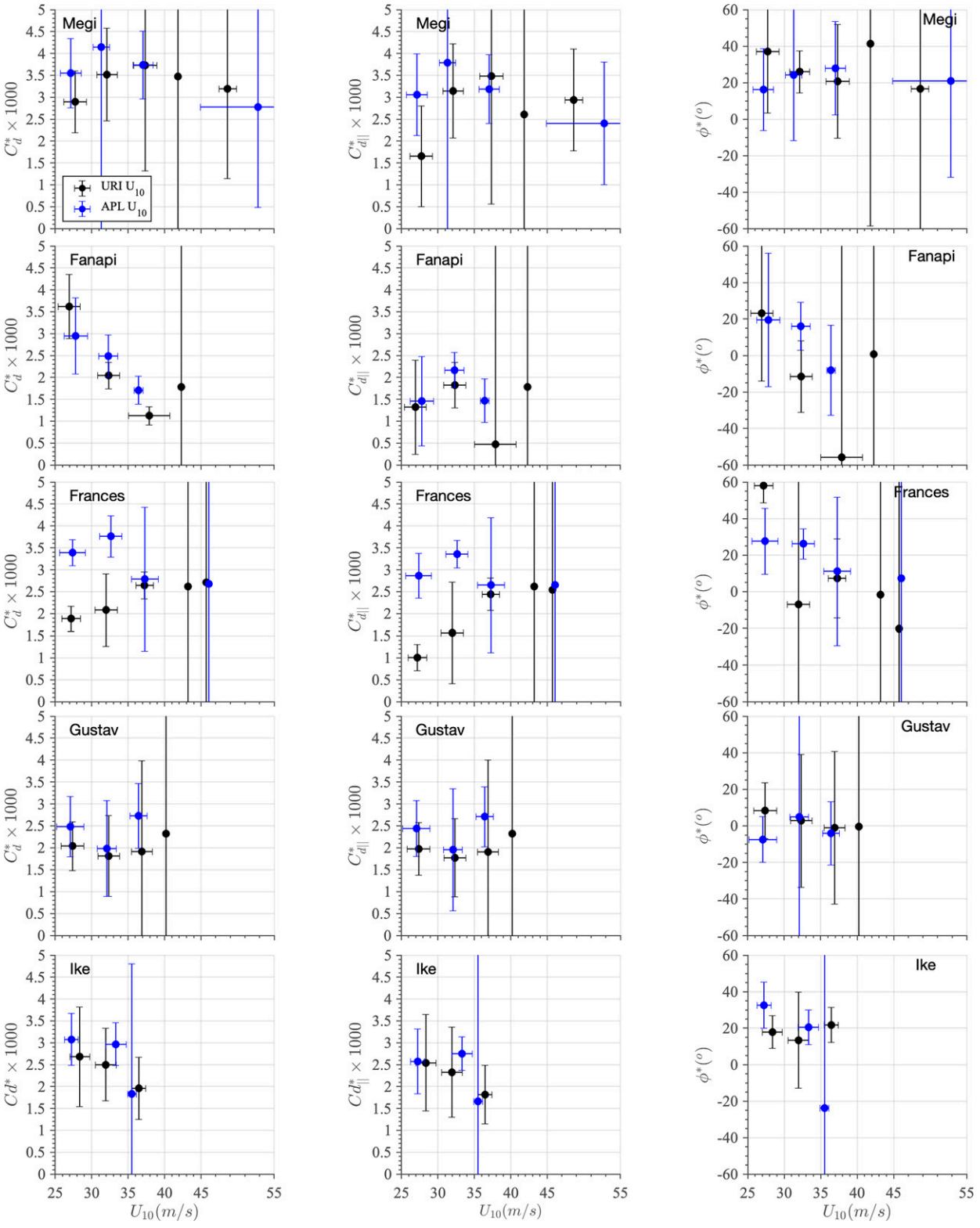

FIG. 11. As in Fig. 10, but separated for each TC and in front-right sector.

Brought to you by NOAA Central Library | Unauthenticated | Downloaded 10/06/22 12:39 PM UTC

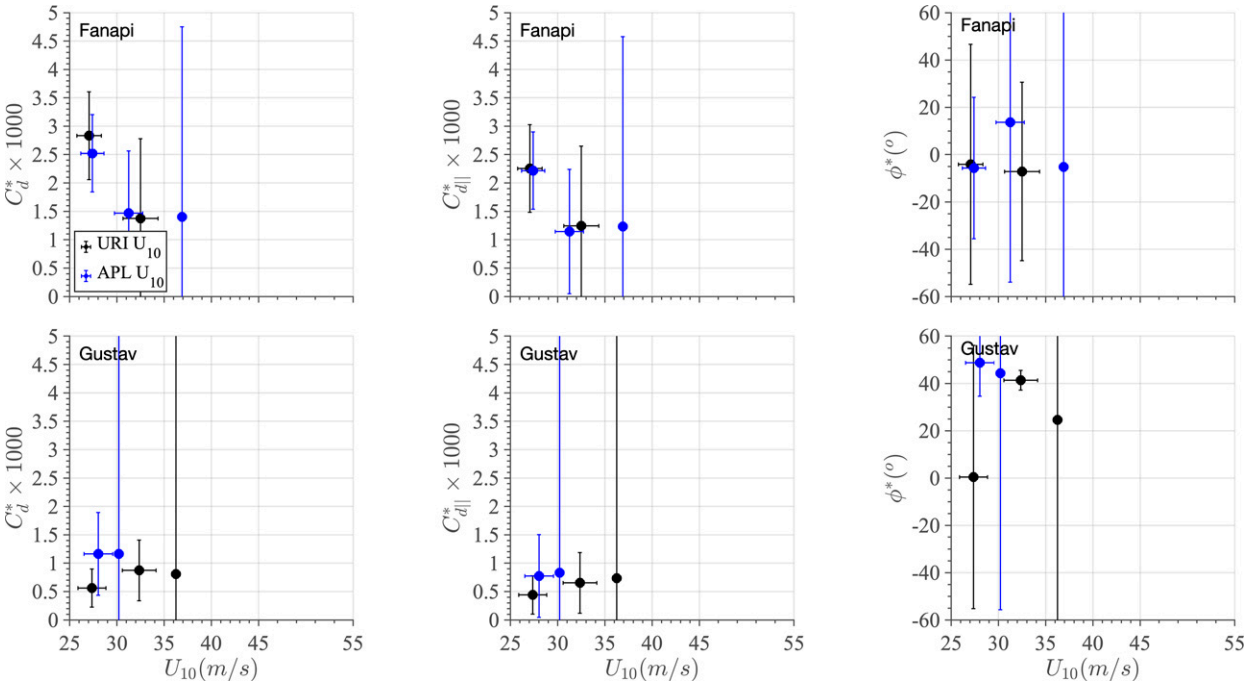

FIG. 12. As in Fig. 10, but separated for each TC and in front-left sector.

objective of this subsection is to examine to what degree the drag coefficient estimates vary because of the wind speed differences among different wind products. Following Hsu et al. (2019) the estimations are made only in front of TCs, and the results are separated into front-right and front-left sectors. There are 109 data points in the front-right sector and 30 data points in the front-left sector under all five TCs, since we have not applied our data quality criteria for this exercise.

In general, the results of C_d^*, $C_{d\|}^*$, and ϕ^* from the two wind products agree reasonably well in both the front-right and front-left sectors (Fig. 10). The vertical error bars (95% confidence) significantly overlap for most data points. This suggests that our drag coefficient estimates are not significantly affected by wind speed uncertainty if a large number of data points are averaged. Notice that both C_d^* and $C_{d\|}^*$ are significantly lower in the front-left sector than in the front-right sector. This is likely because dominant wave direction is more misaligned from wind direction in the front-left sector, as discussed in section 3c. (In front-left and front-right of TCs, roughly 80% and 30% of data show large misalignment angles exceeding 45°, respectively.)

If the results are shown separately for each TC, the difference between the two wind products becomes more noticeable (Figs. 11 and 12). In particular, significant differences appear in lower wind conditions ($|U_{10}| < 30$ m s^{-1}) under Megi and Frances, corresponding to the noticeable differences between the URI and APL wind fields (Fig. 7). The figures also confirm that C_d^* and $C_{d\|}^*$ significantly vary from storm to storm, as pointed out by Hsu et al. (2019). We suspect that the wind speed differences among different wind products is partly responsible for the observed storm dependent variations of C_d^* and $C_{d\|}^*$.

b. *Results of model simulations and data quality control*

An example of observed and simulated wind driven current time series is shown in Fig. 13. We have chosen Float 3763 under Typhoon Megi since it passed under high wind speeds (Fig. 14a). The model simulations generally agree well with the observations. The initial excitation of wind-driven current and its rotation in later times are well reproduced in the simulations. The differences among the four model results (Experiments A–D, discussed in section 3) are subtle, i.e., the surface wave impacts are not large. Note that both the KPP-iLT (Experiment A) and KPP-LT (Experiments B–D) have been tuned against the same set of LES runs including the Langmuir turbulence effects (Reichl et al. 2016b). If the simulation is performed without the enhanced mixing by Langmuir turbulence, the difference is expected to be more significant (Reichl et al. 2016a). The currents in Experiment D (with the wave–current interactions included) appear to be slightly weaker. We will later find that our drag coefficient estimates are slightly larger with Experiment D as a result.

Next, we investigate the results of the data quality control process discussed in section 4c. Five examples (one example from each TC) of the time series of vertically integrated momentum budget terms are presented in Fig. 14. In this figure the dashed cyan, dashed purple, and dashed green lines show the magnitudes of combined linear (first and third) terms, nonlinear (second) term, and pressure gradient (fourth) term, on the right side of Eq. (11), respectively. If these four terms (as vectors) are added, it is equal to the wind stress vector [Eq. (11)], whose magnitude is shown by the solid black line. In addition, the time series of $|\boldsymbol{\sigma}^{\text{obs}}|$ and $|\boldsymbol{\sigma}^{\text{sim}}|$ are shown by the solid gray and solid red lines, respectively.

Brought to you by NOAA Central Library | Unauthenticated | Downloaded 10/06/22 12:39 PM UTC

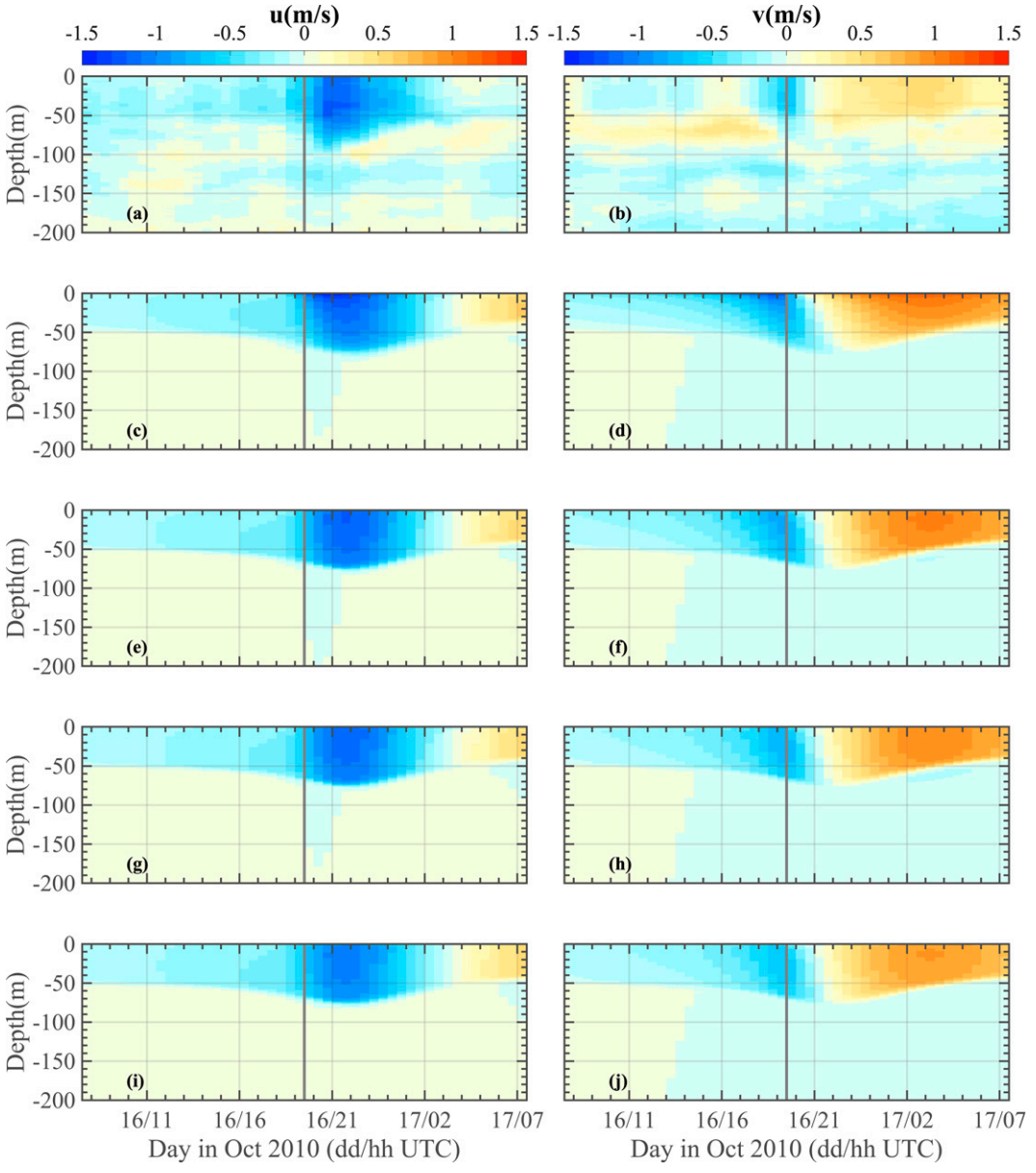

FIG. 13. Time series of (left) zonal velocity u and (right) meridional velocity v of wind driven currents from EM-APEX float 3763 under (a),(b) Megi and from model experiments (c),(d) A; (e),(f) B; (g),(h) C; and (i),(j) D. The gray line indicates time when the storm center was closest to the float array.

Recall that one of our imposed criteria is that $|\boldsymbol{\sigma}^{\text{sim}}|$ (solid red line) is between 70% and 130% of the imposed wind stress magnitude (solid black line). The figure clearly shows that our data quality control process has successfully removed data points when the nonlinear (dashed purple) and/or pressure gradient (dashed green) terms are significant. Even with this strict data control a significant number (195) of data points have been found usable, including many in the rear of storms (positive arrival time in Fig. 14), which are excluded in Hsu et al. (2017, 2019). It is noteworthy that significant differences sometimes appear between the integrated linear terms (dashed cyan) and $|\boldsymbol{\sigma}^{\text{sim}}|$, that is, the time derivative calculated from the two float profiles can be significantly different from the partial time derivative because of the drifting of the float.

c. *Results of drag coefficient*

We now present the results of estimated M_r, C_d, $C_{d\|}$, and ϕ using all 195 data points under five TCs in Fig. 15 (top panels). The magnitude ratio M_r between the observed $|\boldsymbol{\sigma}^{\text{obs}}|$ and the simulated $|\boldsymbol{\sigma}^{\text{sim}}|$ (first panel from left) is reasonably close to 1 except for the highest wind bin of $U_{10} > 45$ m s^{-1}. The number of data points in this bin is small and the error bar is large. (The lower end of the error bar is less than 1.) Therefore, it is

Brought to you by NOAA Central Library | Unauthenticated | Downloaded 10/06/22 12:39 PM UTC

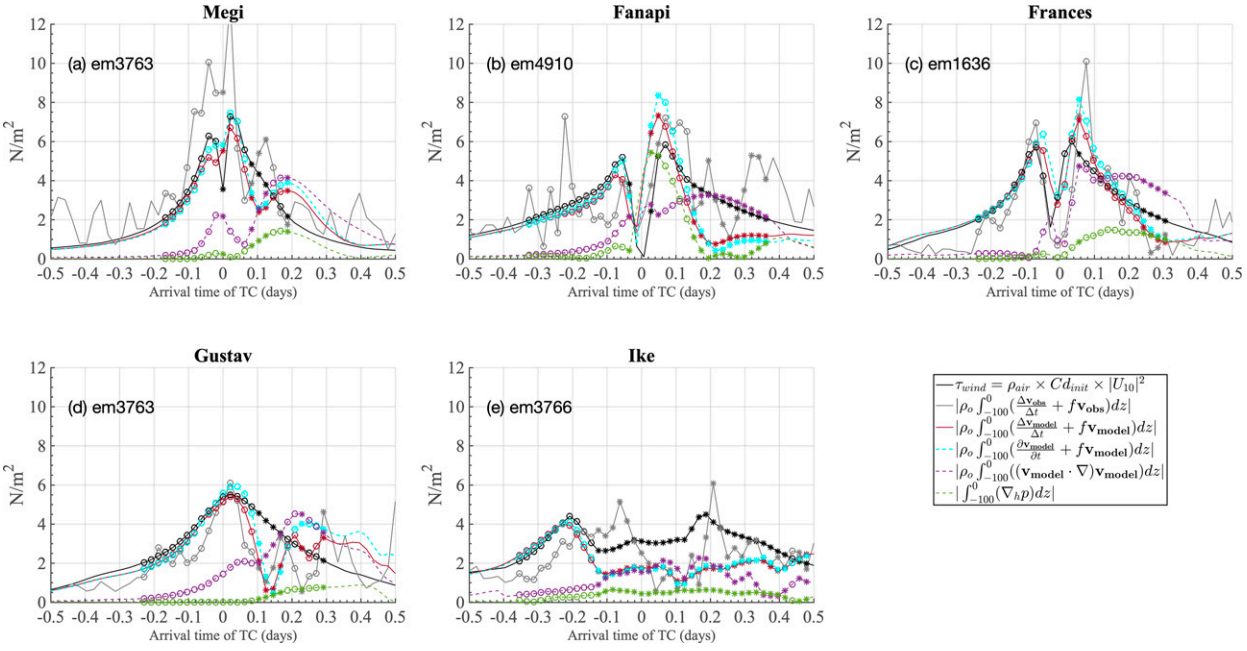

FIG. 14. Time series of momentum budget terms. Black solid line shows imposed wind stress magnitude. Cyan, purple, and green dashed lines show combined linear, nonlinear, and pressure gradient terms (all vertically integrated), respectively. Gray and red solid lines show $\boldsymbol{\sigma}^{\text{obs}}$ and $\boldsymbol{\sigma}^{\text{sim}}$, respectively. Circle symbols indicate data used in this study. Cross symbols indicate data removed by the data quality control process. Float name is labeled in each panel.

not clear whether the difference between $|\boldsymbol{\sigma}^{\text{obs}}|$ and $|\boldsymbol{\sigma}^{\text{sim}}|$ is statistically significant.

Since the result of M_r suggests that the GFDL C_d is reasonably consistent with the observation, we do not repeat the model simulation with a modified C_d^{init}. Instead, the drag coefficient is estimated by multiplying the GFDL C_d and the observed M_r, and is shown in the second panel from the left in Fig. 15. The results confirm that our estimated C_d is close to

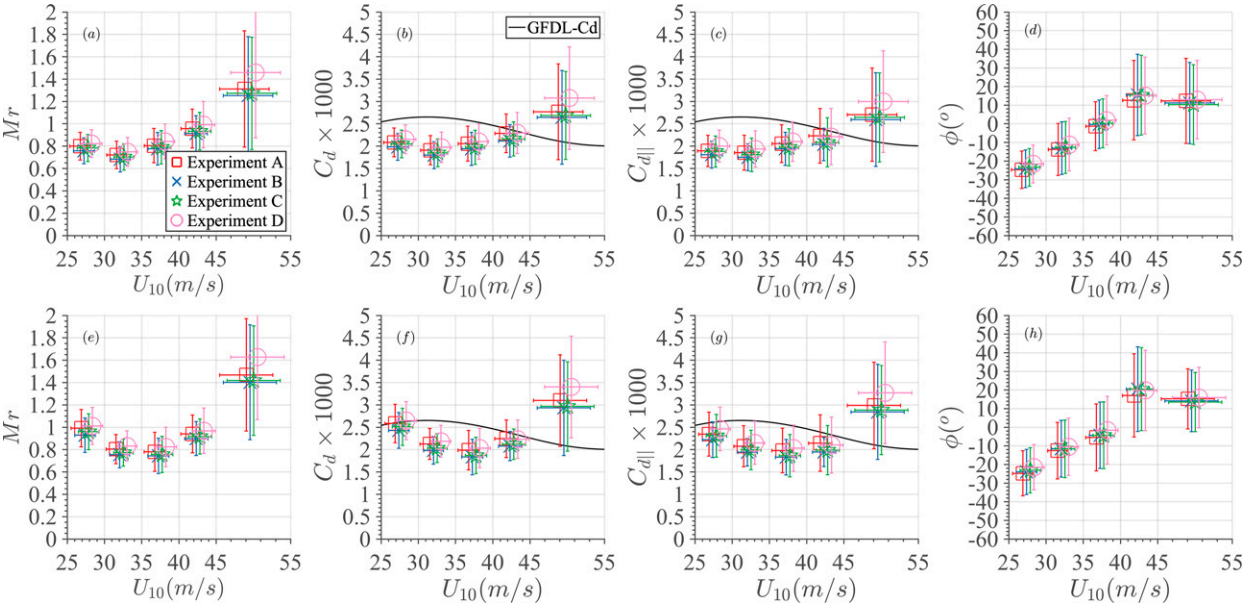

FIG. 15. Bin-averaged estimates of (a) M_r, (b) drag coefficient C_d, (c) along-wind drag coefficient $C_{d||}$, and (d) misalignment angle ϕ between wind stress and wind speed, from five TCs. Different symbols represent results from four model experiments. Black lines indicate GFDL C_d. Horizontal error bars represent the standard deviations of U_{10}. Vertical error bars indicate 95% confidence level. (e)–(h) As in (a)–(d), but exclude data with significantly misaligned swell ($|\psi| > 45°$).

Brought to you by NOAA Central Library | Unauthenticated | Downloaded 10/06/22 12:39 PM UTC

the GFDL C_d. Both our C_d and the GFDL C_d show weak wind speed dependence and their values are mostly in the range of 2–3 $\times 10^{-3}$ for wind speeds 25–55 m s^{-1}. The reasonable agreement between our C_d estimates and the GFDL C_d is particularly encouraging because these two have been derived using completely different approaches; the former is based on in situ upper-ocean observations and the latter is based on a larger number of atmospheric TC simulations (Ginis et al. 2015; Biswas 2018). The observed weak wind speed dependence of our C_d (slight decrease first and then increase with U_{10}) appears to be opposite of that of the GFDL C_d (slight increase first and then decrease with U_{10}), and this C_d trend appears significant because the error bars due to scatter of observational data are relatively small. However, the observed weak C_d trend is likely insignificant because using different wind products can affect the C_d results by 0.5 $\times 10^{-3}$ or more as discussed earlier (also see Fig. 6 in the supplemental material). In addition, we have repeated C_d estimations using more strict and less strict data quality control criteria. While the overall C_d values remain very similar (2–3 $\times 10^{-3}$), the C_d trend can vary depending on the criteria (see supplemental material, Supporting Information C).

The misalignment angle ϕ between $\boldsymbol{\sigma}^{\text{obs}}$ and $\boldsymbol{\sigma}^{\text{sim}}$ is shown in the rightmost panel in Fig. 15. This is an estimate of the misalignment of wind stress direction relative to wind speed direction. Generally, the estimated value is not large. The error bars mostly intersect $\phi = 0°$. However, ϕ tends to be negative (wind stress direction is to the right of wind speed direction) in lower wind speeds. We will later find that the negative ϕ may be related to the negative ψ (dominant wave direction is to the right of wind speed direction), where ψ is the misalignment angle of dominant surface wave direction relative to wind speed direction.

The difference of C_d estimates using the four different experiments (A–D) is mostly negligibly small. Including different surface wave effects does not appear to influence the C_d estimates. The only exception is the highest wind speed bin, where the result of Experiment D is significantly larger than the rest, which is consistent with the earlier observation that the wind driven currents are weaker in Experiment D. This suggests that the wave–current interaction effect can be important in some conditions and that it is desirable to investigate the effect more accurately by modifying the ocean model momentum equations directly, instead of approximating the effect in the boundary conditions as done in this study.

As discussed earlier, our C_d estimates (around 2.7 $\times 10^{-3}$) in the highest wind bin ($U_{10} > 45$ m s^{-1}) is larger than the GFDL C_d (around 2.1 $\times 10^{-3}$). Furthermore, the estimates by Hsu et al. (2017), obtained using the same observational data, are around 2 $\times 10^{-3}$ and are also lower than our estimates. Therefore, we have carefully investigated the possible causes of this difference between our estimate and the estimates by Hsu et al. (2017). The first cause is the difference in the wind fields. Figure 10a shows that the estimates with the URI wind is larger than those with the APL wind by about 0.3 $\times 10^{-3}$. Another cause is the different approaches taken to correct for the nonlinear and pressure gradient terms. Hsu et al. (2017) estimates that this correction reduces the drag coefficient estimates, but our momentum budget analysis under Megi (Fig. 14a) shows that the correction increases the estimates (from solid red line to solid black line) in high-wind conditions. Interestingly, our analyses under Fanapi (Fig. 14b) and Frances (Fig. 14c) show that the correction can be opposite, i.e., can decrease the C_d estimates as in Hsu et al. (2017). (In our analysis of the highest wind bin, four data points come from Megi, two from Frances, and one from Fanapi.) These analyses suggest that both the wind field specification and the C_d estimate correction are difficult to constrain, and that the difference between our C_d estimates and the GFDL C_d or the C_d estimates by Hsu et al. (2017) are not conclusive.

Next, the results of estimated M_r, C_d, $C_{d\|}$, and ϕ are presented separately for each TC in Fig. 16. Although the error bars mostly intersect the GFDL C_d, the estimates appear to vary from storm to storm. In particular, the bin averages under Gustav are significantly below the GFDL C_d. As discussed in section 3a we suspect that this storm dependence is partly due to the wind field uncertainty. It is also possible that some variations are caused by different sea states as discussed in the next section.

Some bin averages show more noticeable differences among the four experiments (A–D), compared to the results combining all TCs in Fig. 15. This suggests that the surface wave effects may impact the upper-ocean responses and the C_d estimates in some cases, but their impacts tend to cancel out if a large number of observations are averaged.

6. Sea state dependence of drag coefficient

In this section we only show the analysis based on the simulation from Experiment C, since the sea state dependence analysis for all 4 experiment are almost identical.

a. *Effect of misaligned swell*

As discussed in section 1 many previous studies suggest that C_d is not a function of U_{10} only, but depends on sea states. In particular, in TC conditions it is common to observe dominant surface waves that propagate in a different direction from the local wind direction (misaligned swell). Both observations (Holthuijsen et al. 2012) and modeling studies (Chen et al. 2013; Reichl et al. 2014; Chen et al. 2020) suggest that the drag coefficient may be strongly influenced by misaligned swell. Note that the term "swell" is used here for waves that are not locally generated. In low to medium wind speeds the wind forcing on swells is weak or even negative. However, swells can be strongly forced by wind in TC conditions if they are aligned with wind.

We first examine the misalignment angle ψ between the dominant wave direction and the wind direction for all the data points. In Fig. 17a the spatial distribution of $|\psi|$ relative to the storm center is shown in the normalized coordinate system, in which the distance from the storm center is normalized by the radius of maximum wind of the TC. As expected, the misalignment is mostly small to the right and right rear of the storm, but is large in the far front (approximately >2–3$R_{\max}$) and in the left-front quadrant, often exceeding 45°.

Brought to you by NOAA Central Library | Unauthenticated | Downloaded 10/06/22 12:39 PM UTC

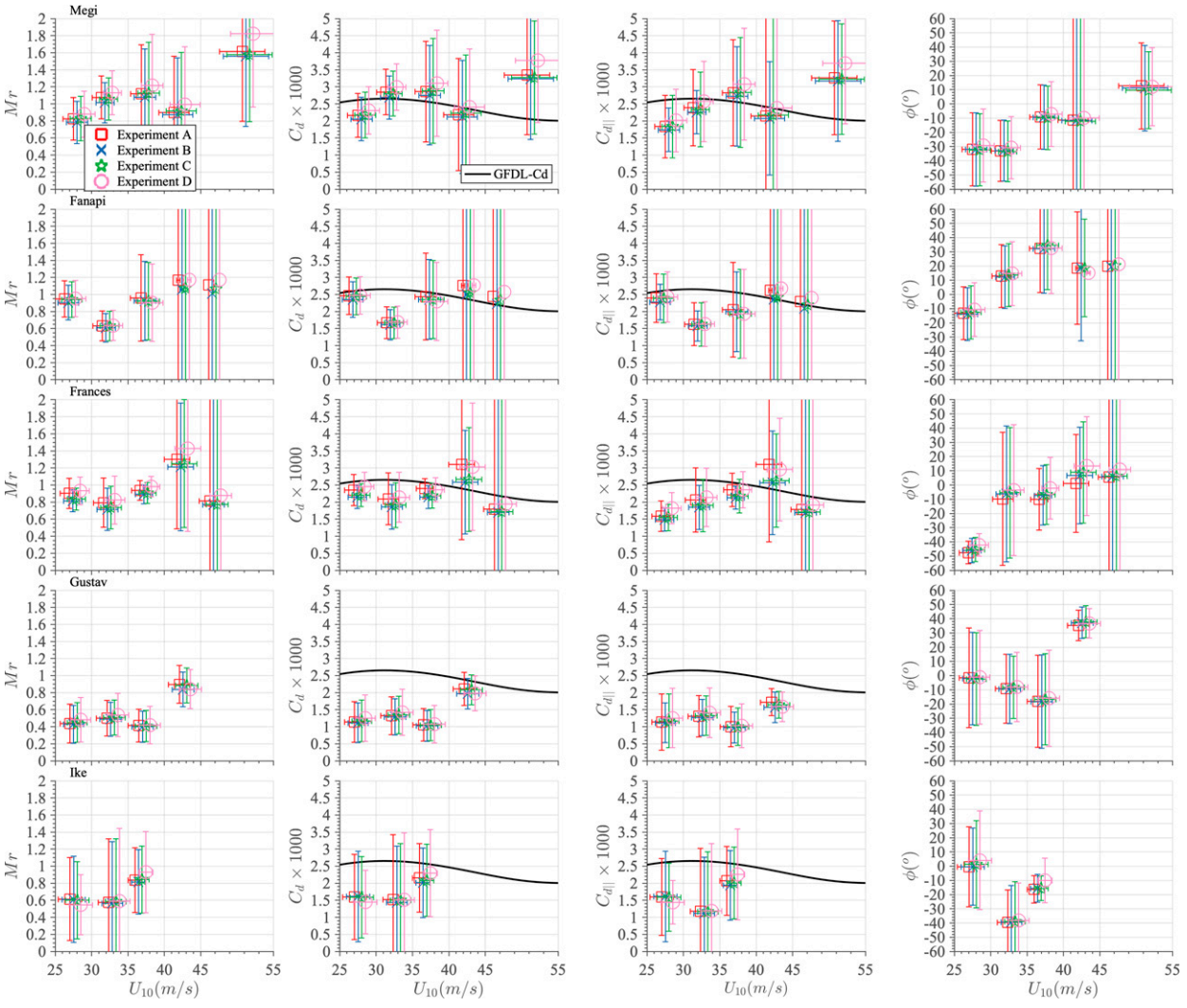

FIG. 16. As in the top panels of Fig. 15, but separated for each TC.

In Fig. 18 the dependence of C_d, Z_{ch}, and ϕ on the misalignment angle $|\psi|$ is presented. The data are bin averaged every 22.5° increment of $|\psi|$ for each wind speed bin (color coded filled circles). For C_d and ϕ the bin averages are also shown for all wind speeds combined (black empty squares). The two data points with $|\psi| > 90°$ are excluded. One immediately notices that both C_d and Z_{ch} rapidly decrease as $|\psi|$ exceeds around 45°. This strongly suggests that dominant waves misaligned by more than 45° from wind have a negative impact on the drag coefficient. The existing models of sea state–dependent drag coefficient (Chen et al. 2013; Reichl et al. 2014; Chen et al. 2020) also predict slight reduction of C_d as the misalignment angle $|\psi|$ increases because the form drag of swell decreases. However, the observed reduction of C_d is significantly stronger than the model predictions.

With smaller misalignment between dominant waves and wind speed ($|\psi| < 45°$), the misalignment ϕ between the wind stress and wind speed scatter above and below 0°, but ϕ becomes more consistently negative for $|\psi| > 45°$. We find that significantly misaligned dominant waves ($|\psi| > 45°$) almost always propagate to the right of wind ($\psi < -45°$). Therefore, there appears to be some correlation between the negative ψ and negative ϕ, that is, misaligned swell propagating to the right of wind tend to turn the wind stress direction to the right toward the swell direction. This is qualitatively consistent with previous modeling studies (Chen et al. 2013; Reichl et al. 2014; Chen et al. 2020).

As discussed earlier, large misalignment $|\psi| > 45°$ mainly occurs in the far front and in the left-front quadrant (Fig. 17a), where the drag coefficient appears to be reduced according to Fig. 18a. This particular spatial dependence of $|\psi|$ is a possible reason why C_d in the previous study (Hsu et al. 2019) and our C_d^* estimates (section 3a) show significant spatial dependence, i.e., they are lower in the far front and in the left-front quadrant.

Since large misalignment $|\psi| > 45°$ is common under TCs, it is likely that misaligned swells contribute to overall reduction of the mean drag coefficient averaged over all sea states. In

Brought to you by NOAA Central Library | Unauthenticated | Downloaded 10/06/22 12:39 PM UTC

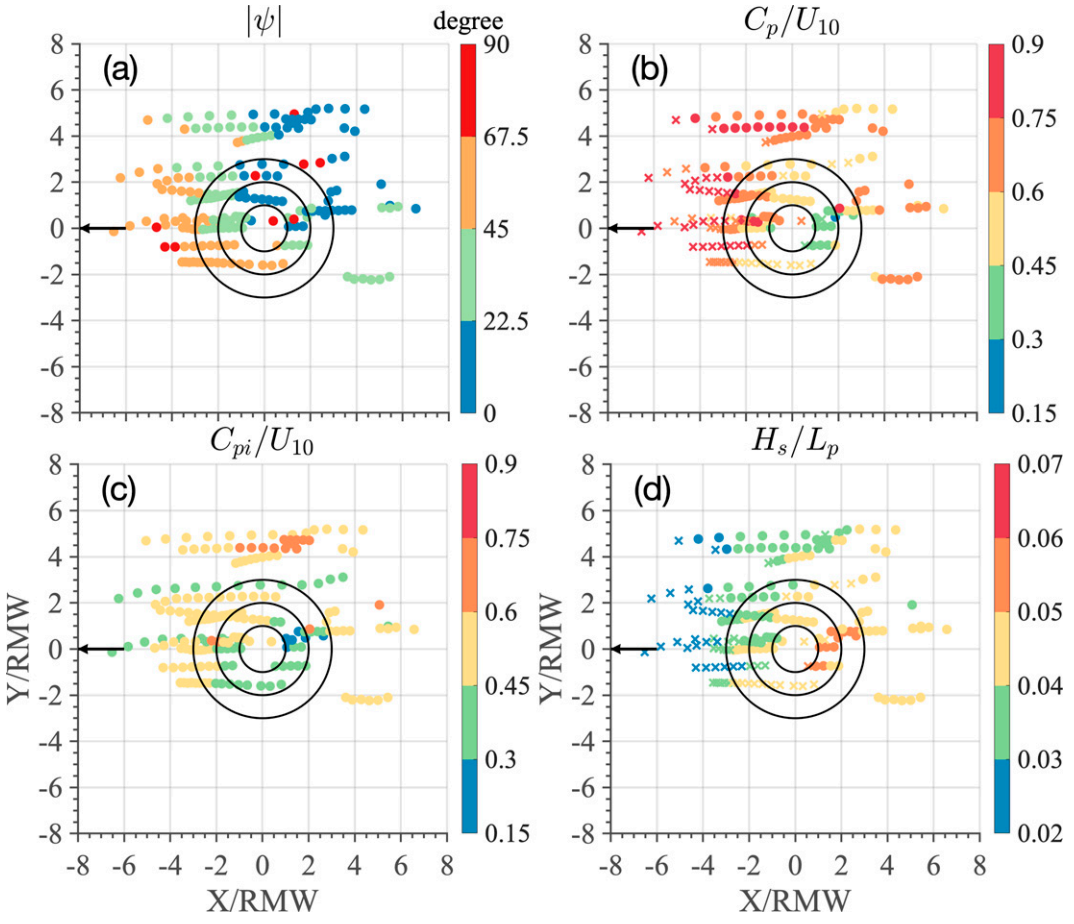

FIG. 17. Spatial distribution of misalignment angle $|\psi|$ between dominate waves and (a) wind, (b) wave age C_p/U_{10}, (c) input wave age C_{pi}/U_{10}, and (d) wave steepness H_s/L_p. Cross symbols in (b) and (d) indicate data with significantly misaligned swell $|\psi| > 45°$. Solid black circles show $R_{\max}$, $2 \times R_{\max}$, and $3 \times R_{\max}$. Storms propagate to the left.

Fig. 15 (bottom panels) we recalculate M_r, C_d, $C_{d\|}$, and ϕ under all five TCs excluding the misaligned swell data with $|\psi| > 45°$. (The number of data points is decreased from 195 to 129). As expected, M_r, C_d, and $C_{d\|}$ all increase compared to the results including misaligned swell (top panels). This suggests that common occurrence of misaligned swell may be partially responsible for the overall reduction of the drag coefficient under TCs. We also find that the observations under

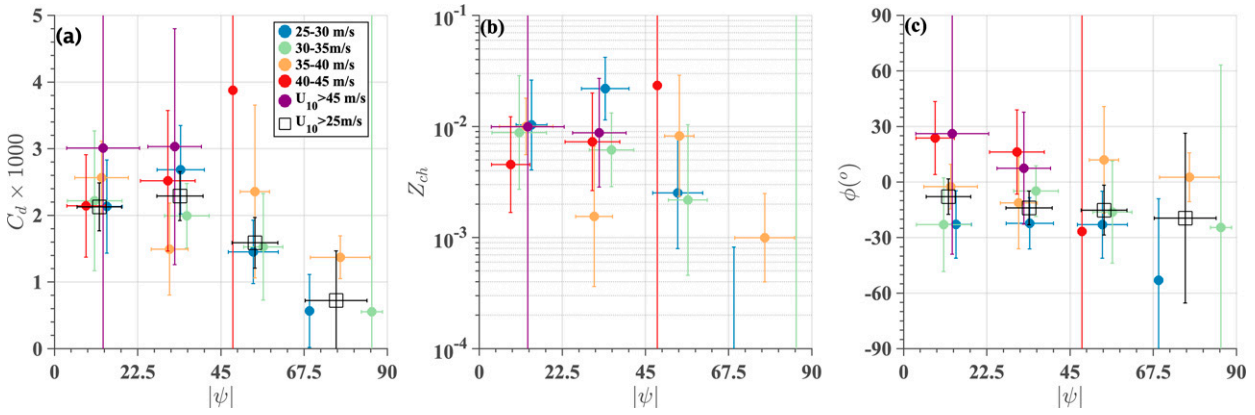

FIG. 18. Bin-averaged estimates of (a) C_d, (b) Charnock coefficient Z_{ch}, and (c) misalignment angle ϕ between wind stress and wind speed, plotted against misalignment angle $|\psi|$ between dominate waves and wind speed.

Brought to you by NOAA Central Library | Unauthenticated | Downloaded 10/06/22 12:39 PM UTC

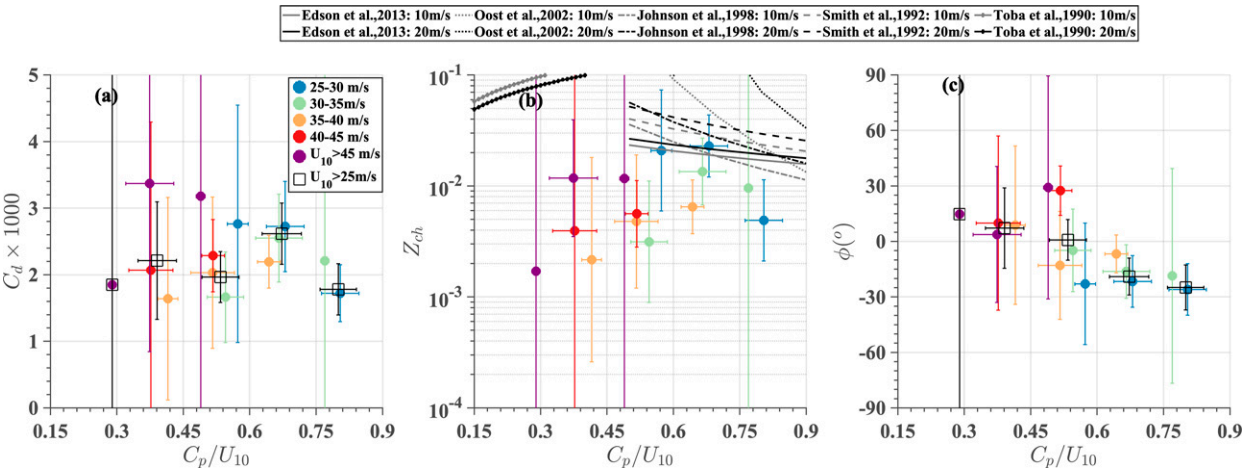

FIG. 19. Bin-averaged estimates of (a) C_d, (b) Charnock coefficient Z_{ch}, and (c) misalignment angle ϕ between wind stress and wind speed, plotted against wave age C_p/U_{10}. Different lines show previously reported relationships between Z_{ch} and C_p/U_{10}, as labeled. Data with significantly misaligned swell $|\psi| > 45°$ are excluded.

Hurricane Gustav contain many data points with large misalignment $|\psi| > 45°$ in lower winds, and they likely contribute to the reduced C_d (Fig. 16).

b. *Dependence of drag coefficient on wave age and wave steepness*

The common parameters to distinguish different sea states in previous studies include wave steepness H_s/L_p, wave age c_p/u_*, and input wave age c_{pi}/u_*, where c_{pi} is the input phase speed at the input peak frequency that is determined by wind energy input calculated in WW3. Unlike c_p, c_{pi} excludes the contribution from waves that are not wind forced (e.g., swell in low to medium winds, significantly misaligned swell in TCs). Therefore, c_{pi} is always smaller than c_p but it becomes close to c_p in pure wind seas.

In this subsection we investigate the dependence of the estimated C_d, Z_{ch}, and ϕ on these sea state parameters. To avoid the self-correlation due to the large scatter of u_*, we redefine the wave age and input wave age as c_p/U_{10}, and c_{pi}/U_{10}, respectively.

The spatial distribution of c_p/U_{10}, c_{pi}/U_{10}, and H_s/L_p are shown in Figs. 17b–d, respectively. In the plots of c_p/U_{10} and H_s/L_p distributions, data points with large misalignment $|\psi| > 45°$ are marked by crosses instead of circles, and are excluded in the analyses of c_p/U_{10} dependence and H_s/L_p dependence. However, we retain these data in the analysis of c_{pi}/U_{10} dependence because the input wave age should be able to exclude the contamination from misaligned swell.

Figure 17b shows that larger wave ages are more common from the front left to the right of the storm, frequently with misaligned dominant waves, while young seas appear just behind the storm. The distribution of the input wave age in Fig. 17c shows that the wind sea part of the wave spectrum (locally wind forced waves) is mostly young (input wave age less than 0.6). The wave steepness H_s/L_p appears to be inversely correlated with the wave age c_p/U_{10} (cf. Figs. 17b,d), and the steepest waves appear just behind the storm.

In Fig. 19 the observed dependence of C_d, Z_{ch}, and ϕ on the wave age c_p/U_{10} is presented. Recall that the data points with significantly misaligned swell are excluded. The data are bin averaged every 0.15 increment of c_p/U_{10} for each wind speed bin (color coded filled circles). For C_d and ϕ the bin averages are also shown for all wind speeds combined (black empty squares). As expected, the wave age itself is strongly correlated with wind speed (Fig. 20a). Seas tend to be younger in higher wind speeds. Therefore, it is not easy to distinguish the dependence on c_p/U_{10} from the dependence on U_{10}. Nevertheless, for older seas ($c_p/U_{10} > 0.6$) both C_d and Z_{ch} appear to decrease with the wave age c_p/U_{10}, even within the same wind bins. In particular, the dependence of Z_{ch} on c_p/U_{10} at the lowest wind bin (blue) appear quite similar to the dependence observed in previous studies in low to medium wind conditions (Smith et al. 1992; Johnson et al. 1998; Oost et al. 2002; Edson et al. 2013). Note that the parameterizations proposed in the previous studies based on c_p/u_* have been converted to those based on c_p/U_{10} in Fig. 19b. The misalignment angle ϕ becomes significantly negative with increasing wave age for older seas ($c_p/U_{10} > 0.5$) (Fig. 19c). Although we have removed the data points with significantly misaligned swell ($|\psi| > 45°$) in this analysis, older seas often contain dominant waves propagating to the right of wind (misaligned by less than 45°) and may contribute to the turning of the wind stress direction to the right.

Interestingly, the dependence of C_d and Z_{ch} on the wave age c_p/U_{10} seems to disappear or even be reversed, i.e., they may increase with increasing c_p/U_{10} if seas are younger ($c_p/U_{10} < 0.6$). Such young waves are rarely observed in low to medium wind speeds; they are observed only with very short fetch, such as in laboratory wind wave flumes. However, they are quite common in TC winds. Although this increasing dependence of Z_{ch} with increasing c_p/U_{10} is qualitatively consistent with the parameterization by Toba et al. (1990), which is based on combined field and laboratory observations in low to medium wind speeds, our observed Z_{ch} values are

Brought to you by NOAA Central Library | Unauthenticated | Downloaded 10/06/22 12:39 PM UTC

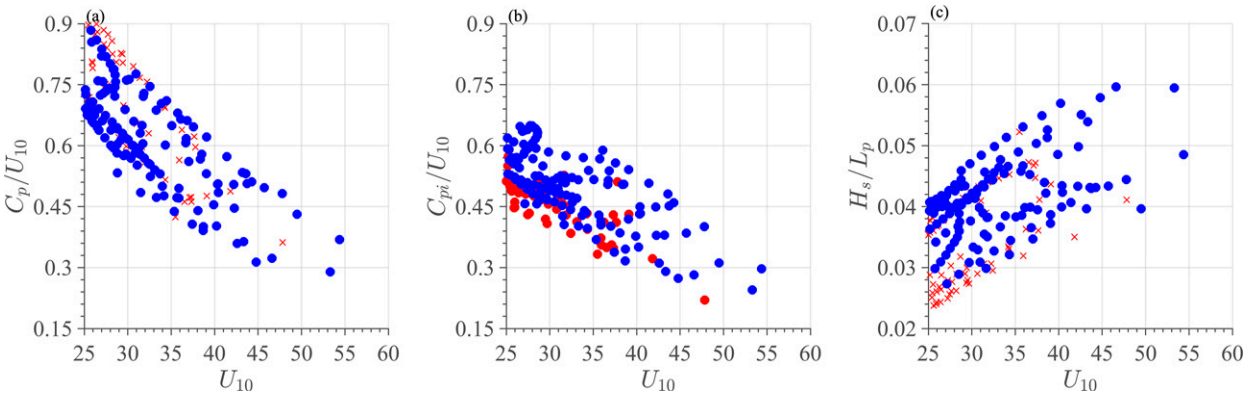

FIG. 20. (a) Wave age C_p/U_{10}, (b) input wave age C_{pi}/U_{10}, and (c) wave steepness H_s/L_p, plotted against wind speed U_{10}. The red filled circles (included in Fig. 21) and red crosses (excluded in Figs. 19 and 22) indicate data with $|\psi| > 45°$, while the blue filled circles are data with $|\psi| \leq 45°$.

significantly lower. This suggests that the high-wind TC conditions and strongly forced laboratory conditions are very different regimes (the same parameterization does not apply).

We next investigate the observed dependence of C_d, Z_{ch}, and ϕ on the input wave age c_{pi}/U_{10} in Fig. 21. Recall that we have now included the data points with significantly misaligned swell. Since c_{pi}/U_{10} is always smaller than c_p/U_{10}, the overall range of c_{pi}/U_{10} is significantly narrower than that of c_p/U_{10}. Nevertheless, we still observe strong correlation between c_{pi}/U_{10} and U_{10} (Fig. 20b); the wind sea part of wave spectrum is younger with higher wind speed. As in the case of wave age dependence, C_d and Z_{ch} seem to remain constant or slightly increase with the input wave age c_{pi}/U_{10} for younger seas. However, their overall dependence on c_{pi}/U_{10} is weak, that is, c_{pi}/U_{10} does not show clear sea state dependence in this wind speed range.

Last, the dependence of C_d, Z_{ch}, and ϕ on the wave steepness H_s/L_p is shown in Fig. 22. Here, the data with significantly misaligned swell have been excluded. The steepness H_s/L_p is also correlated with wind speed U_{10}; steeper waves tend to occur under stronger winds.

In the lowest wind bin (blue) both C_d and Z_{ch} appear to increase with increasing H_s/L_p. The dependence of Z_{ch} is roughly consistent with the previous parameterizations by Edson et al. (2013) and Taylor and Yelland (2001), based on observations in low to medium wind speeds. However, both C_d and Z_{ch} appear to remain flat or even decrease with increasing H_s/L_p in higher wind speeds (even within the same wind speed bin). Generally, the steepness H_s/L_p does not collapse the data very well and at least within our dataset.

7. Summary and concluding remarks

a. *Summary of the study*

In this study the drag coefficient (C_d) and its sea state dependence under TCs were investigated by combining upper-ocean current observations and a coupled ocean–wave (MOM6–WW3) simulations. The current observations were

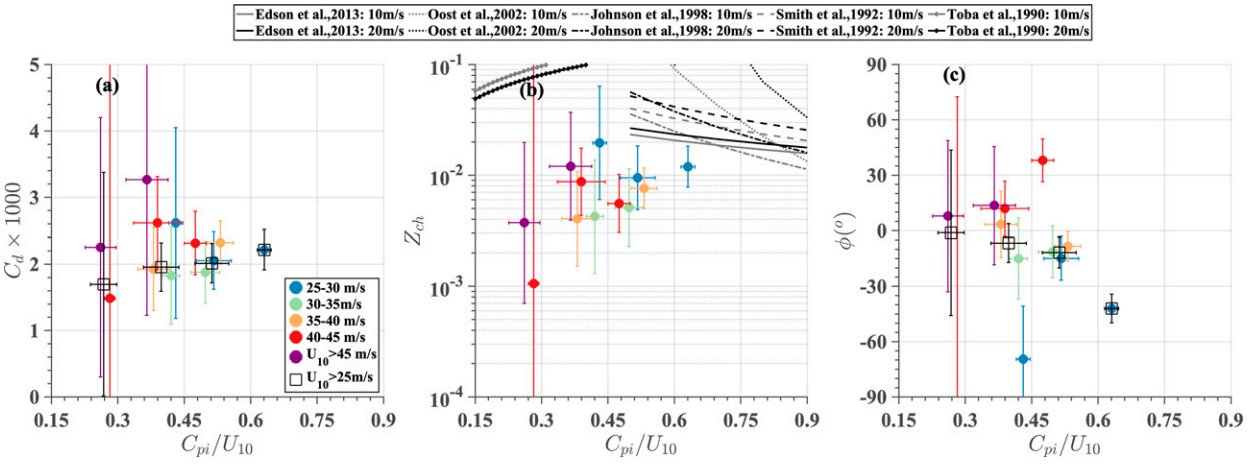

FIG. 21. Bin-averaged estimates of (a) C_d, (b) Charnock coefficient Z_{ch}, and (c) misalignment angle ϕ between wind stress and wind speed, plotted against input wave age C_{pi}/U_{10}. Different lines show previously reported relationships between Z_{ch} and C_p/U_{10}, as labeled. Data with significantly misaligned swell $|\psi| > 45°$ are included.

Brought to you by NOAA Central Library | Unauthenticated | Downloaded 10/06/22 12:39 PM UTC

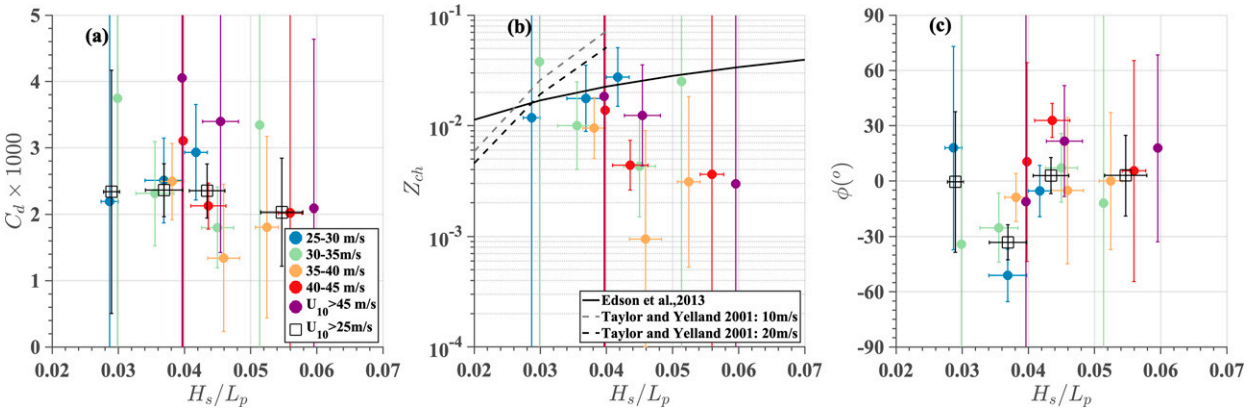

FIG. 22. Bin-averaged estimates of (a) C_d, (b) Charnock coefficient Z_{ch}, and (c) misalignment angle ϕ between wind stress and wind speed, plotted against wave steepness H_s/L_p. Different lines show previously reported relationships between Z_{ch} and H_s/L_p, as labeled. Data with significantly misaligned swell $|\psi| > 45°$ are excluded.

made using EM-APEX floats deployed under five TCs: Typhoon Megi (2010), Typhoon Fanapi (2010), Hurricane Frances (2004), Hurricane Gustav (2008), and Hurricane Ike (2008).

In the previous study (Hsu et al. 2019), which utilized the same ocean current observations, the wind stress was initially estimated from the vertical integral of two linear terms in the ocean current momentum equation, and was later corrected for the contribution from the neglected terms. In this study the MOM6–WW3 model was run to simulate the observed conditions using an assumed drag coefficient, and the drag coefficient was estimated for each float observation based on direct comparison between the observed and simulated ocean currents. This approach made it possible to utilize many data points behind the storm, to investigate the sea state dependence of C_d in detail, and to investigate different surface wave impacts (Langmuir turbulence, air–sea momentum flux budget, wave–current interactions) on the upper-ocean currents and the C_d estimates.

The estimated drag coefficient averaged over all TCs is consistent with the GFDL drag coefficient (Ginis et al. 2015), which is used as the assumed C_d in the model simulations. Both our estimated C_d and the GFDL C_d are in the range of 2–3 $\times$ 10^{-3} for wind speeds of 25–55 m s^{-1}, and show weak wind speed dependence. This result is encouraging because the two drag coefficients have been obtained by completely different approaches: our C_d is based on the upper-ocean current observations, while the GFDL C_d is based on a large number of atmospheric model simulations of TCs. We find significant storm dependence of the estimated C_d. We suspect that this is partly due to wind speed differences among different wind products under TC conditions. However, averaging over a large number of observations seems to minimize the impact of wind speed differences on the C_d estimates.

One of the most significant findings in this study is that C_d is significantly reduced by misaligned swell, that is, if the misalignment angle ψ between the dominant wave direction and the wind direction exceeds about 45°. Since misaligned swell is common in the far front and in the front-left quadrant of the storm, C_d tends to be lower in the same areas, and displays a distinct spatial distribution pattern as suggested by the previous study (Hsu et al. 2019). Our results also suggest that common occurrence of misaligned swell may be partially responsible for the overall reduction of C_d under TC conditions. Misaligned swell also appears to turn the wind stress direction toward the swell direction from the wind direction.

In lower wind bins (25–30 m s^{-1}) our estimates of the drag coefficient and the Charnock coefficient Z_{ch} decrease with increasing wave age c_p/U_{10}. These trends are roughly consistent with previous observations made in low to medium wind speeds. However, in higher wind speed bins these trends disappear or even are reversed, that is, C_d and Z_{ch} may increase with increasing wave age c_p/U_{10}. We find that the input wave age c_{pi}/U_{10} and the wave steepness H_s/L_p do not distinguish different sea state effects at least within our dataset. These results are not conclusive because of the limited number of observational data. More observations are needed to refine such sea state–dependence analyses.

We find that the different surface wave effects (Langmuir turbulence, air–sea momentum flux budget, wave–current interactions) on upper-ocean currents/turbulence generally have minor impacts on the overall C_d estimates. However, the wave–current interactions may have large impacts on the upper-ocean responses and the C_d estimates in some conditions.

Finally, we have confirmed that our conclusions of the mean C_d values as well as their dependence on sea states remain valid even if all the analyses are performed using a different wind product (see Supporting Information E in the supplemental material for more details).

b. *Concluding remarks*

Based on the findings discussed above, the two key conclusions from this study are as follows:

1) If a large number of data are averaged, the drag coefficient C_d is around 2–3 $\times$ 10^{-3} and depends on wind speed only weakly in the range of U_{10} between 25 and 55 m s^{-1}.

Brought to you by NOAA Central Library | Unauthenticated | Downloaded 10/06/22 12:39 PM UTC

2) However, C_d is more strongly dependent on sea states in the same wind speed range. In particular, this study clearly demonstrates that misaligned swell significantly reduces C_d, a feature which is underestimated by current models of sea state–dependent drag coefficient.

The second conclusion strongly suggests that it is beneficial to implement an improved sea state–dependent parameterization of the drag coefficient in TC conditions.

Some previous studies suggest that the drag coefficient parameterization should depend on storm relative locations. While our analyses do show spatial patterns of the swell misalignment angle ψ and other sea state parameters, it is unclear whether such an approach can fully capture significant sea state dependence. The simple quadrant analysis (front left, front right, etc.) is clearly insufficient.

Proposed alternative approaches are to estimate the sea state parameters based on the storm parameters (e.g., radius of maximum wind, maximum wind speed, storm translation speed) without running a wave model, such as using the effective wind duration parameter proposed by Hsu et al. (2019). We have found that this particular parameter is not able to distinguish the swell misalignment angle ψ and the resulting C_d variation very well. Nevertheless, it may be possible to develop an alternative approach focused on accurately predicted ψ.

However, the sea state dependence of C_d is expected to be complex. For example, the effect of misaligned swell may not depend on ψ alone, but may also depend on steepness and phase speed (relative to wind) of the swell. Therefore, it is likely more beneficial to couple a wave model and a hurricane (either atmosphere only or atmosphere plus ocean) model and introduce a sea state–dependent parameterization of C_d based on the full wave spectrum.

Finally, developing such a parameterization requires better understanding of how misaligned swell reduces C_d, based on more observational and theoretical/numerical studies, because existing models clearly underestimate this impact.

Acknowledgments. We acknowledge support of the National Science Foundation (Physical Oceanography) Grant OCE1756164. We also acknowledge high-performance computing support from Cheyenne (doi:10.5065/D6RX99HX) provided by NCAR's Computational and Information Systems Laboratory, sponsored by the National Science Foundation. IG was supported by a grant from the Ministry of Ocean and Fisheries, Korea, URI Award AWD06003. The versions of MOM6 and WAVEWATCH III used in this work are derived from open-source codes available at github.com/NOAA-GFDL/MOM6 and github.com/NOAA-EMC/WW3/. We thank Drs. Kun Gao and Raphael Dussin for their comments on drafts of this paper. We thank Dr. Xuanyu Chen for her help of validating WW3 performance. Finally, we acknowledge the contribution (EM-APEX data) of Thomas Sanford. This work would not have been possible without him.

Data availability statement. The model simulation and processed EM-APEX dataset in this study can be accessed by request from the Mendeley data repository (via doi:10.17632/gnc6hz2nwm.1).

REFERENCES

Adcroft, A., and Coauthors, 2019: The GFDL global ocean and sea ice model OM4.0: Model description and simulation features. *J. Adv. Model. Earth Syst.*, **11**, 3167–3211, https://doi.org/10.1029/2019MS001726.

Biswas, M., and Coauthors, 2018: Hurricane Weather Research and Forecasting (HWRF) Model: 2018 scientific documentation. Development Testbed Centre Rep., 103 pp., https://dtcenter.org/sites/default/files/community-code/hwrf/docs/scientific_documents/HWRFv4.0a_ScientificDoc.pdf.

Black, P. G., and Coauthors, 2007: Air–sea exchange in hurricanes: Synthesis of observations from the coupled boundary layer air–sea transfer experiment. *Bull. Amer. Meteor. Soc.*, **88**, 357–374, https://doi.org/10.1175/BAMS-88-3-357.

Bryant, K. M., and M. Akbar, 2016: An exploration of wind stress calculation techniques in hurricane storm surge modeling. *J. Mar. Sci. Eng.*, **4**, 58, https://doi.org/10.3390/jmse4030058.

Charnock, H., 1955: Wind stress on a water surface. *Quart. J. Roy. Meteor. Soc.*, **81**, 639–640, https://doi.org/10.1002/qj.49708135027.

Chen, S. S., W. Zhao, M. A. Donelan, and H. L. Tolman, 2013: Directional wind–wave coupling in fully coupled atmosphere–wave–ocean models: Results from CBLAST-hurricane. *J. Atmos. Sci.*, **70**, 3198–3215, https://doi.org/10.1175/JAS-D-12-0157.1.

Chen, X., I. Ginis, and T. Hara, 2018: Sensitivity of offshore tropical cyclone wave simulations to spatial resolution in wave models. *J. Mar. Sci. Eng.*, **6**, 116, https://doi.org/10.3390/jmse6040116.

——, ——, and ——, 2020: Impact of shoaling ocean surface waves on wind stress and drag coefficient in coastal waters: 2. Tropical cyclones. *J. Geophys. Res. Oceans*, **125**, e2020JC016223, https://doi.org/10.1029/2020JC016223.

D'Asaro, E. A., 2014: Turbulence in the upper-ocean mixed layer. *Annu. Rev. Mar. Sci.*, **6**, 101–115, https://doi.org/10.1146/annurev-marine-010213-135138.

Donelan, M. A., B. K. Haus, N. Reul, W. J. Plant, M. Stiassnie, H. C. Graber, O. B. Brown, and E. S. Saltzman, 2004: On the limiting aerodynamic roughness of the ocean in very strong winds. *Geophys. Res. Lett.*, **31**, L18306, https://doi.org/10.1029/2004GL019460.

Edson, J. B., and Coauthors, 2013: On the exchange of momentum over the open ocean. *J. Phys. Oceanogr.*, **43**, 1589–1610, https://doi.org/10.1175/JPO-D-12-0173.1.

Fan, Y., I. Ginis, T. Hara, C. W. Wright, and E. J. Walsh, 2009: Numerical simulations and observations of surface wave fields under an extreme tropical cyclone. *J. Phys. Oceanogr.*, **39**, 2097–2116, https://doi.org/10.1175/2009JPO4224.1.

——, ——, and ——, 2010: Momentum flux budget across the air–sea interface under uniform and tropical cyclone winds. *J. Phys. Oceanogr.*, **40**, 2221–2242, https://doi.org/10.1175/2010JPO4299.1.

Ginis, I., M. Bender, B. Thomas, M. Morin, V. Tallapragada, and A. Soloviev, 2015: A new drag coefficient formulation and its impact on the GFDL and HWRF hurricane model predictions. *19th Conf. on Air-Sea Interaction*, Phoenix, AZ, Amer. Meteor. Soc., 5.4, https://ams.confex.com/ams/95Annual/webprogram/Paper268750.html.

Brought to you by NOAA Central Library | Unauthenticated | Downloaded 10/06/22 12:39 PM UTC

Harper, B., J. Kepert, and J. Ginger, 2010: Guidelines for converting between various wind averaging periods in tropical cyclone conditions. WMO/TD-1555, World Meteorological Organization, 54 pp., https://library.wmo.int/doc_num.php?explnum_id=290.

Holthuijsen, L. H., M. D. Powell, and J. D. Pietrzak, 2012: Wind and waves in extreme hurricanes. *J. Geophys. Res.*, **117**, C09003, https://doi.org/10.1029/2012JC007983.

Hsu, J.-Y., R.-C. Lien, E. A. D'Asaro, and T. B. Sanford, 2017: Estimates of surface wind stress and drag coefficients in Typhoon Megi. *J. Phys. Oceanogr.*, **47**, 545–565, https://doi.org/10.1175/JPO-D-16-0069.1.

——, ——, ——, and ——, 2019: Scaling of drag coefficients under five tropical cyclones. *Geophys. Res. Lett.*, **46**, 3349–3358, https://doi.org/10.1029/2018GL081574.

Johnson, H. K., J. Højstrup, H. J. Vested, and S. E. Larsen, 1998: On the dependence of sea surface roughness on wind waves. *J. Phys. Oceanogr.*, **28**, 1702–1716, https://doi.org/10.1175/1520-0485(1998)028<1702:OTDOSS>2.0.CO;2.

Large, W. G., and S. Pond, 1981: Open ocean momentum flux measurements in moderate to strong winds. *J. Phys. Oceanogr.*, **11**, 324–336, https://doi.org/10.1175/1520-0485(1981)011<0324:OOMFMI>2.0.CO;2.

Liu, Q., A. Babanin, Y. Fan, S. Zieger, C. Guan, and I.-J. Moon, 2017: Numerical simulations of ocean surface waves under hurricane conditions: Assessment of existing model performance. *Ocean Modell.*, **118**, 73–93, https://doi.org/10.1016/j.ocemod.2017.08.005.

Moon, I.-J., I. Ginis, T. Hara, H. L. Tolman, C. Wright, and E. J. Walsh, 2003: Numerical simulation of sea surface directional wave spectra under hurricane wind forcing. *J. Phys. Oceanogr.*, **33**, 1680–1706, https://doi.org/10.1175/2410.1.

Oost, W., G. Komen, C. Jacobs, and C. Van Oort, 2002: New evidence for a relation between wind stress and wave age from measurements during ASGAMAGE. *Bound.-Layer Meteor.*, **103**, 409–438, https://doi.org/10.1023/A:1014913624535.

PopStefanija, I., C. W. Fairall, and E. J. Walsh, 2021: Mapping of directional ocean wave spectra in hurricanes and other environments. *IEEE Trans. Geosci. Remote Sens.*, **59**, 9007–9020, https://doi.org/10.1109/TGRS.2020.3042904.

Powell, M. D., P. J. Vickery, and T. A. Reinhold, 2003: Reduced drag coefficient for high wind speeds in tropical cyclones. *Nature*, **422**, 279–283, https://doi.org/10.1038/nature01481.

Price, J. F., R. A. Weller, and R. Pinkel, 1986: Diurnal cycling: Observations and models of the upper ocean response to diurnal heating, cooling, and wind mixing. *J. Geophys. Res.*, **91**, 8411–8427, https://doi.org/10.1029/JC091iC07p08411.

Reichl, B. G., T. Hara, and I. Ginis, 2014: Sea state dependence of the wind stress over the ocean under hurricane winds. *J. Geophys. Res. Oceans*, **119**, 30–51, https://doi.org/10.1002/2013JC009289.

——, I. Ginis, T. Hara, B. Thomas, T. Kukulka, and D. Wang, 2016a: Impact of sea-state-dependent Langmuir turbulence on the ocean response to a tropical cyclone. *Mon. Wea. Rev.*, **144**, 4569–4590, https://doi.org/10.1175/MWR-D-16-0074.1.

——, D. Wang, T. Hara, I. Ginis, and T. Kukulka, 2016b: Langmuir turbulence parameterization in tropical cyclone conditions. *J. Phys. Oceanogr.*, **46**, 863–886, https://doi.org/10.1175/JPO-D-15-0106.1.

Sanford, T. B., J. F. Price, and J. B. Girton, 2011: Upper-ocean response to Hurricane Frances (2004) observed by profiling EM-APEX floats. *J. Phys. Oceanogr.*, **41**, 1041–1056, https://doi.org/10.1175/2010JPO4313.1.

Shearman, R., and A. Zelenko, 1989: Wind measurements reduction to a standard level. WMO/TD-311, MMROA Rep. 22, World Meteorological Organization, 23 pp.

Smith, J. A., 2006: Wave–current interactions in finite depth. *J. Phys. Oceanogr.*, **36**, 1403–1419, https://doi.org/10.1175/JPO2911.1.

Smith, S. D., and Coauthors, 1992: Sea surface wind stress and drag coefficients: The hexos results. *Bound.-Layer Meteor.*, **60**, 109–142, https://doi.org/10.1007/BF00122064.

Soloviev, A. V., R. Lukas, M. A. Donelan, B. K. Haus, and I. Ginis, 2014: The air-sea interface and surface stress under tropical cyclones. *Sci. Rep.*, **4**, 5306, https://doi.org/10.1038/srep05306.

Suzuki, N., and B. Fox-Kemper, 2016: Understanding Stokes forces in the wave-averaged equations. *J. Geophys. Res. Oceans*, **121**, 3579–3596, https://doi.org/10.1002/2015JC011566.

Taylor, P. K., and M. J. Yelland, 2001: The dependence of sea surface roughness on the height and steepness of the waves. *J. Phys. Oceanogr.*, **31**, 572–590, https://doi.org/10.1175/1520-0485(2001)031<0572:TDOSSR>2.0.CO;2.

Toba, Y., N. Iida, H. Kawamura, N. Ebuchi, and I. S. F. Jones, 1990: Wave dependence of sea-surface wind stress. *J. Phys. Oceanogr.*, **20**, 705–721, https://doi.org/10.1175/1520-0485(1990)020<0705:WDOSSW>2.0.CO;2.

Tsujino, H., and Coauthors, 2018: JRA-55 based surface dataset for driving ocean–sea-ice models (JRA55-do). *Ocean Modell.*, **130**, 79–139, https://doi.org/10.1016/j.ocemod.2018.07.002.

Walsh, E., D. Hancock III, D. Hines, R. Swift, and J. Scott, 1985: Directional wave spectra measured with the surface contour radar. *J. Phys. Oceanogr.*, **15**, 566–592, https://doi.org/10.1175/1520-0485(1985)015<0566:DWSMWT>2.0.CO;2.

Walsh, E. J., D. Hancock, D. E. Hines, R. N. Swift, and J. F. Scott, 1987: Wave-measurement capabilities of the surface contour radar and the airborne oceanographic lidar. *Johns Hopkins APL Tech. Dig.*, **8**, 74–81, https://www.jhuapl.edu/Content/techdigest/pdf/V08-N01/08-01-Walsh.pdf

——, D. W. Hancock III, D. E. Hines, R. N. Swift, and J. F. Scott, 1989: An observation of the directional wave spectrum evolution from shoreline to fully developed. *J. Phys. Oceanogr.*, **19**, 670–690, https://doi.org/10.1175/1520-0485(1989)019<0670:AOOTDW>2.0.CO;2.

——, and Coauthors, 2002: Hurricane directional wave spectrum spatial variation at landfall. *J. Phys. Oceanogr.*, **32**, 1667–1684, https://doi.org/10.1175/1520-0485(2002)032<1667:HDWSSV>2.0.CO;2.

Wright, C. W., and Coauthors, 2001: Hurricane directional wave spectrum spatial variation in the open ocean. *J. Phys. Oceanogr.*, **31**, 2472–2488, https://doi.org/10.1175/1520-0485(2001)031<2472:HDWSSV>2.0.CO;2.

WW3DG, 2019: User manual and system documentation of WAVEWATCH III version 6.07. WAVEWATCH III Development Group, Tech. Note 333, 465 pp.

Brought to you by NOAA Central Library | Unauthenticated | Downloaded 10/06/22 12:39 PM UTC